Remote Sensing of Environment 258 (2021) 112396

Contents lists available at ScienceDirect

Remote Sensing of Environment

journal homepage: www.elsevier.com/locate/rse

Assessing the impact of illumination on UAV pushbroom hyperspectral imagery collected under various cloud cover conditions

J. Pablo Arroyo-Mora [a,*], Margaret Kalacska [b], Trond Løke [c], Daniel Schläpfer [d], Nicholas C. Coops [e], Oliver Lucanus [b], George Leblanc [a]

[a] National Research Council of Canada, Flight Research Laboratory, 1920 Research Rd., Ottawa, ON, Canada
[b] Applied Remote Sensing Laboratory (ARSL), Department of Geography, McGill University, Montreal, QC, Canada
[c] Norsk Elektro Optikk AS, Prost Stabels vei 22, 2019 Skedsmokorset, Norway
[d] ReSe Applications LLC, Langeggweg 3, CH-9500 Wil, Switzerland
[e] Integrated Remote Sensing Studio (IRSS), Faculty of Forestry, University of British Columbia, 2424 Main Mall, Vancouver, BC, Canada

ARTICLE INFO

Keywords:
Drones
Hyperspectral
Atmospheric compensation
Signal to noise ratio
Spectral vegetation indices
Garry oak

ABSTRACT

The recent development of small form-factor (<6 kg), full range (400–2500 nm) pushbroom hyperspectral imaging systems (HSI) for unmanned aerial vehicles (UAV) poses a new range of opportunities for passive remote sensing applications. The flexible deployment of these UAV-HSI systems have the potential to expand the data acquisition window to acceptable (though non-ideal) atmospheric conditions. This is an important consideration for time-sensitive applications (e.g. phenology) in areas with persistent cloud cover. Since the majority of UAV studies have focused on applications with ideal illumination conditions (e.g. minimal or non-cloud cover), little is known to what extent UAV-HSI data are affected by changes in illumination conditions due to variable cloud cover. In this study, we acquired UAV pushbroom HSI (400–2500 nm) over three consecutive days with various illumination conditions (i.e. cloud cover), which were complemented with downwelling irradiance data to characterize illumination conditions and in-situ and laboratory reference panel measurements across a range of reflectivity (i.e. 2%, 10%, 18% and 50%) used to evaluate reflectance products. Using these data we address four fundamental aspects for UAV-HSI acquired under various conditions ranging from high (624.6 ± 16.63 W·m^2) to low (2.5 ± 0.9 W·m^2) direct irradiance: atmospheric compensation, signal-to-noise ratio (SNR), spectral vegetation indices and endmembers extraction. For instance, two atmospheric compensation methods were applied, a radiative transfer model suitable for high direct irradiance, and an Empirical Line Model (ELM) for diffuse irradiance conditions. SNR results for two distinctive vegetation classes (i.e. tree canopy vs herbaceous vegetation) reveal wavelength dependent attenuation by cloud cover, with higher SNR under high direct irradiance for canopy vegetation. Spectral vegetation index (SVIs) results revealed high variability and index dependent effects. For example, NDVI had significant differences ($p < 0.05$) across illumination conditions, while NDWI appeared insensitive at the canopy level. Finally, often neglected diffuse illumination conditions may be beneficial for revealing spectral features in vegetation that are obscured by the predominantly non-Lambertian reflectance encountered under high direct illumination. To our knowledge, our study is the first to use a full range pushbroom UAV sensor (400–2500 nm) for assessing illumination effects on the aforementioned variables. Our findings pave the way for understanding the advantages and limitations of ultra-high spatial resolution full range high fidelity UAV-HSI for ecological and other applications.

1. Introduction

In many regions of the world, persistent cloud cover poses significant challenges for the acquisition of useful terrestrial optical remotely sensed imagery (e.g. Asner, 2001; Basnet and Vodacek, 2015; Sano et al., 2007). Globally, the average daily cloud fraction over land estimated from the Moderate Resolution Imaging Spectroradiometer (MODIS) over 12 years of continuous observations from Terra and over nine years from Aqua is ~55%, with a distinct seasonal cycle (King et al., 2013). As a result, methodologies for the detection and masking of clouds and cloud

* Corresponding author.
E-mail address: juanpablo.arroyo-mora@nrc-cnrc.gc.ca (J.P. Arroyo-Mora).

https://doi.org/10.1016/j.rse.2021.112396
Received 5 June 2020; Received in revised form 22 February 2021; Accepted 7 March 2021
Available online 17 March 2021

shadows, including accounting for haze, are required but can greatly reduce the area suitable for analyses in a given image (Frantz et al., 2018; Richter, 1996; Zhu and Woodcock, 2012). The recent implementation of unmanned aerial vehicle hyperspectral imaging systems (UAV-HSI) (e.g. Arroyo-Mora et al., 2019; Lucieer et al., 2014; Zarco-Tejada et al., 2013) allows for the possibility of acquiring ultra-high spatial (cm) and temporal resolution imagery at low altitudes below low-level cloud formations (Wang et al., 2019), providing novel opportunities for optical remote sensing studies.

While many studies list the range of applications to which the rapidly growing field of UAV imagery has been applied, recent work with UAV platforms has also investigated foundational aspects of application independent, assessments of vegetation properties and acquisition parameters, at ultra-fine spatial scales, such as the Bidirectional Reflectance Distribution Function (BRDF) (e.g. Burkart et al. (2015)), albedo (e.g. Levy et al. (2018)), and leaf-area-index (LAI) (Potgieter et al., 2017; Yao et al., 2017). However, these studies are similar to the majority of optical remote sensing studies in that they have been acquired under ideal clear sky conditions. As a result of the near exclusive use of clear skies, the potential utility of HSI collected under non-ideal conditions (i.e. cloudy conditions when diffuse skylight dominates), requires further study. Because consistent, direct illumination has been considered essential for several optical remote sensing applications, the main limiting factor for UAV data acquisition has remained variable weather conditions (Banerjee et al., 2020; Hakala et al., 2013; Ranquist et al., 2017). However, the few studies which investigate HSI acquired under diffuse illumination conditions below clouds have shown great potential; for example, the BRDF reduces to a hemispherical-directional observation situation (i.e. Hemispherical-Directional Reflectance Factor: HDRF. Nicodemus et al. (1977)) at almost isotropic illumination conditions.

The majority of studies assessing the impact of illumination conditions due to differences in cloud cover on UAV acquired imagery data have used RGB Structure-from-Motion photogrammetry. For example, Wierzbicki et al. (2015) found that while cloudy conditions with fog deteriorate the quality of the digital elevation model and orthomosaics, a modified flight plan increasing photograph overlap could mitigate the problems reasonably well. Ruwaimana et al. (2018) found improved classification of mangrove species from RGB mosaics acquired under cloudy conditions than from high spatial resolution satellite imagery due to reduced glare from the water, higher spatial resolution (cm vs 2 m) and homogenous illumination with minimal shadows. Notably fewer studies have examined UAV multispectral or HSI under cloudy or variable irradiance. For example, Wang et al. (2019) developed a tensor decomposition to produce repeatable reflectance time series under variable and low irradiance conditions from UAV multispectral imagery with applications to high latitudes and persistently cloudy tropical regions. Some of the earliest studies examining HSI under non-ideal illumination conditions are Hakala et al. (2013), Honkavaara et al. (2013) and Honkavaara and Khoramshahi (2018) who implemented and refined a radiometric block adjustment using in -situ irradiance measurements to produce normalized imagery across flight lines collected under varying illumination conditions due to persistent and variable cloud cover with a tunable Fabry-Pérot Interferometer. Similarly, Li et al. (2015) found that an irradiance sensor based atmospheric compensation of a pushbroom VNIR (380 and 1000 nm) UAV-HSI produced better results in comparison to a radiative transfer model-based approach when the aerosol type was difficult to determine. However, additional studies addressing variable illumination conditions of full range (400–2500 nm) pushbroom UAV-HSI of natural targets and real in-situ conditions are required for understanding the full potential these systems have for a wide range of applications. Because HSI resolves the electromagnetic spectrum at a finer detail than multispectral imagery (i.e. larger number of narrower bands), residual features can remain in the data after pre-processing (e.g. errors in radiometric or atmospheric compensation or incomplete removal of atmospheric scattering or absorption features). From multispectral imagery the broader bands may not acquire data spanning specific atmospheric absorption features or if they do, the features may not be visible in the spectra due to the relatively wide bands. As such, the pre-processing of HSI is more sensitive to the environmental conditions under which it was acquired. Moreover, for better implementation in many applications, the ultra-high spatial resolution and high dimensionality of UAV-HSI requires revisiting foundational aspects of passive remote sensing (e.g. illumination, instrument signal-to-noise ratio (SNR), vegetation indices, etc.).

In this study, our objective was to analyze the effects of various illumination conditions due specifically to cloud cover on four aspects of full range (400–2500 nm) pushbroom UAV-HSI: determination of bottom of the atmosphere reflectance, the signal-to-noise ratio (SNR), spectral vegetation indices (SVIs) and scene derived endmembers. First, with the increasing availability of UAV-HSI, there is a need to determine the utility of low altitude full range HSI acquired under cloudy conditions for which no accurate physical inversion based on radiative transfer models alone is feasible. Use of in-situ reflectance measurements of calibrated field panels (e.g. Arroyo-Mora et al., 2019; Lucieer et al., 2014) and downwelling irradiance sensors (Hakala et al., 2013; Li et al., 2015) have been shown to mitigate the effect of the atmosphere on surface reflectance estimation by reducing residual atmospheric artifacts (Soffer et al., 2019; Wang et al., 2019). Second, larger SNR results in more useful information that can be differentiated from the noise inherent in all electro-optical instruments. For many applications, a minimum SNR is required to draw inferences based on the signal originating from the material of interest (e.g. relationship between SVIs and foliar biochemistry, classification, etc.) (Goetz and Calvin, 1987; Moses et al., 2012; Smith and Curran, 1996). Third, commonly used SVIs such as NDVI reduce atmospheric and illumination effects due to the division of spectral bands (Meyer et al., 1995; Rouse Jr. et al., 1974). However, because the most common SVIs were developed for satellite-based Earth observation, the illumination effects they intend to minimize are due to changes in solar zenith angles across latitudes (Rouse Jr. et al., 1974), rather than the differences in direct and diffuse illumination encountered under varying cloud cover. Finally, many conventional endmember identification techniques do not account for major contributing factors to the spectral variability induced by canopy architecture, leaf orientation, irradiance geometry and residual absorption and scattering properties of the atmosphere due to imperfect atmospheric compensation (Adams et al., 1995; Zare and Ho, 2014; Zhang and Du, 2012). There are usually more endmembers than materials in an HSI, due to both environmental/biophysical variations (e.g. different pigment concentrations) as well as illumination (and atmospheric) induced differences and BRDF effects. This property can be exploited to reveal differences in the proportional contribution of environmental/biophysical versus illumination/atmospheric drivers of multiple endmembers within the scene (Gruninger et al., 2004) as a result of irradiance conditions.

To quantitatively assess the effect of various illumination conditions (e.g. clear sky, cloudy and variable cloud cover) on the aforementioned variables, we acquired UAV-HSI during a three day period that were complemented with downwelling irradiance measurements (i.e. pyranometer) for quantifying irradiance, as well as measurements of calibrated standard reference targets of different reflectance levels (Soffer et al., 2019). Our study leads to an improved understanding of how environmental acquisition conditions impact image quality for vegetated areas, especially when considering the VNIR and SWIR spectrum (400–2500 nm). This is especially important for broadening the acquisition window to acceptable (though non-ideal) atmospheric conditions, for time-sensitive, short-lived ecological phenomena of endangered species (e.g. flowering) or environments with persistent cloud cover (e.g. high latitudes, tropical forests, etc.).

2. Methods

2.1. Study area

Garry Oak (*Quercus garryana* Douglas ex Hook.) ecosystems are highly endangered with only 1–5% remaining in a near-natural condition, with a very high diversity of associated plants, (694 plant taxa recorded to date) (Fuchs, 2001). Invasive species, fire suppression regimes, disease and habitat loss are major threats to the survival of Garry Oaks in their natural habitat (Fuchs, 2001; McCune et al., 2013). Our study site is the Cowichan Garry Oak Preserve (CGOP) near Duncan, British Columbia, Canada. The weather here is considered cool and cloudy as is common in the coastal lowlands (McMinn et al., 1976). The CGOP is characterized by a Garry Oak meadow, with a relatively open forest and an understory composed of native grasses and herbaceous vegetation, which follow a distinct phenological pattern with a very short flowering period during the month of May (Supplementary Video 1). Mapping this short flowering event is important to assess the extent of the fragile and endangered herbaceous vegetation and overall ecosystem health. In addition, tree bark and branches are covered by bryophytes and lichen at different densities and form an important component of the tree structure. Because many of the rare herbaceous species (e.g. *Castilleja levisecta, Triteleia howellii*) have short flowering periods (1–2 weeks), the persistent cloud cover presents a challenge to conventional remote sensing approaches.

2.2. Mission planning and ancillary data acquisition

Given the time sensitive nature of the flowering period at the CGOP, a flight plan was developed to maximize UAV-HSI acquisition for specific areas of interest encompassing both Garry oak trees and herbaceous vegetation field plots. UAV-HSI imagery was acquired under various illumination conditions including sunny, homogenous cloud cover and variable cloud cover encountered from May 15th - 17th, 2019. For the meadow, all HSI imagery was acquired at 60 m AGL with a 1 m/s flight speed. Three flight lines were acquired on both May 15th (3500 m^2), and 16th (4700 m^2), with two lines acquired on May 17th (3700 m^2) (Table 1). For the boresight calibration area (see Section 2.3) four flight lines were acquired on May 14th, 2019 at 120 m altitude AGL and 1 m/s flight speed (Fig. 1 inset B). The geocorrected and mosaicked (see Section 2.3) flight lines from the meadow are shown in Fig. 1.

A range of cloud cover conditions are typically encountered in May at the CGOP, therefore, in order to characterize illumination conditions, global and diffuse downwelling irradiance ($W{\cdot}m^{-2}$) measurements were acquired with an SPN1 Sunshine Pyrometer (Delta-T Devices, Cambridge, UK) (spectral range: 400–2700 nm), mounted on a horizontal aluminum bar on a tripod at approximately 140 cm above the ground (Fig. 2). The SPN1 has a resolution of 0.6 $W{\cdot}m^{-2}$, and an overall accuracy of ±8%. The measurement interval for the SPN1 was set to 10 s to capture fine temporal variations in illumination conditions. A Canon EOS60D camera with an ultra-wide-angle lens (Sigma 4.5 mm F2.8 Ex DC Hyper Sonic Motor Circular Fisheye lens) on an intervalometer was also affixed to the opposite end of the horizontal tripod bar to acquire photographs of the sky conditions (Fig. 2). The pyranometer data were collected only to quantify and describe the overall illumination conditions, but were not used in the atmospheric compensation methods (Section 2.5).

Four standard reference panels consisting of 2% and 50% Spectralon™ (25 × 25 cm), a 10% Permaflect™ (50 × 50 cm) panel, and an 18% Flexispec™ (50 × 50 cm) sheet, (Arroyo-Mora et al., 2019; Soffer et al., 2019) (Fig. 2) were set up in the meadow in open areas as far from the trees as possible. However, given the fragile nature of the herbaceous vegetation and the time constraint of the UAV-HSI flights, complete isolation of the panels from in-scattering was not possible (Fig. 2, Supplementary Videos 2 and 3). An ASD FieldSpec 3 (Malvern Panalytical, Boulder, CO, USA) spectroradiometer (2 m fiber extension) was used to measure the in-situ reflectance of the panels relative to a new 99% reflective Spectralon™ panel which had been characterized with respect to a NIST traceable standard and processed via the panel substitution method (Soffer et al., 2019). The estimated absolute reflectance of the panels was calculated via a custom MATLAB toolbox (Elmer et al., 2020). Unfortunately, on May 15th, (sunny conditions) there was no suitable location for the panels within the planned flight lines and therefore, they were placed outside (Fig. 1).

Digital surface models (DSM) were created through Structure-from-Motion Multiview Stereo photogrammetry (SfM-MVS) (Arroyo-Mora et al., 2019; Kalacska et al., 2017; Kalacska et al., 2020) for use in the boresight calibration and geocorrection of the meadow imagery (see Section 2.3), following the methodology described in Kalacska et al. (2020) and Lucanus and Kalacska (2020).

2.3. UAV hyperspectral system (UAV-HSI) and processing to geocorrected radiance

The hyperspectral system consisted of a Mjolnir VS-620 (HySpex NEO, Skedsmokorset Norway) mounted on an octocopter with an H16 XL gimbal (Gremsy, Ho Chi Minh City, Viet Nam) for stabilization. The Mjolnir VS-620 is comprised of two pushbroom hyperspectral imagers (V-1240 and S-620 combined spanning the 400–2500 nm range) (Table 2, Fig. 3), an Inertial Navigation System (INS) (APX-15, Applanix, Richmond Hill ON, Canada), a data acquisition unit (DAU), a data link to a ground station and a custom printed circuit board to control the components including the mechanical shutters, triggering, events, INS interface and external system control. To minimize coregistration errors in the along-track direction the two optical axes are co-aligned. A common trigger is used for both imagers, scaled down by a factor 2 for the S-620, resulting in a VNIR image with twice the resolution. The INS is boresight calibrated, meaning that the translation (xyz) and rotation (wpk) between the imagers' coordinate system and the IMU coordinate system have previously been determined, simplifying direct georeferencing (i.e. no ground control points). Dark current pixels are acquired before and after each imaging flight line and interpolated in processing for every frame (row) in the image.

Direct georeferencing of the imagery (i.e. from position and attitude data rather than ground control points) (e.g. Arroyo-Mora et al., 2019; Freitas et al., 2018), was possible due to 1) accurate time recording of every frame, 2) good INS solution, which includes to a pixel-level or better, fast INS alignment and results minimally impacted by vibration from the UAV or pulse width modulation (PWM) noise, 3) use of a high spatial resolution DSM (see Section 2.2), 4) high accuracy sensor model which is the off-nadir look angle of each pixel determined with a resolution of 0.79 arcsec, and 5) an automatic boresight calibration (Freitas et al., 2018) following (Schläpfer, 2018; Schläpfer and Richter, 2002) carried out in PARGE v3.5®(ReSe, Wil, Switzerland).

Table 1
UAV-HSI meadow flight line characteristics across dates. The illumination condition acronyms refer to SUN for clear sky conditions (May 15th), DIFF for cloudy conditions (May 16th) and VAR for variable illumination (May 17th) during HSI data acquisition.

Date	Illumination condition	Area (m^2)	V-1240 int. time (ms)	S-620 int. time (ms)	Speed (m/s)	Altitude (m)	Solar zenith (°)	Solar azimuth (°)
May 15	High Direct (SUN)	3500	15.5	31.8	1	60	33.3	212.7
May 16	High Diffuse (DIFF)	4700	15.5	31.8	1	60	30.6	162.2
May 17	Variable (VAR)	3700	15.5	31.8	1	60	56.7	98.5

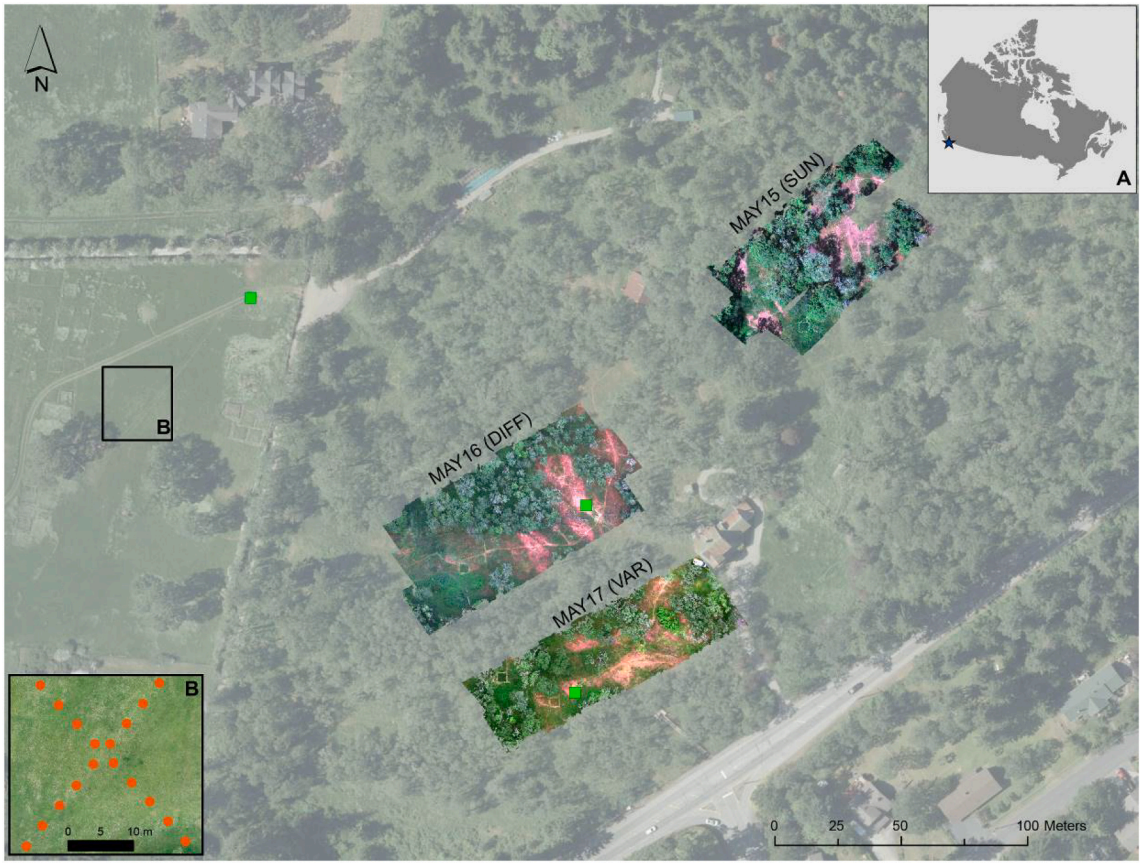

Fig. 1. Meadow section of the Cowichan Garry Oak Preserve (CGOP) with hyperspectral mosaics (true color band combination R: 641 nm, G: 549 nm, B: 461 nm) for imagery acquired May 15–17, 2019. Green squares correspond to the location of reference targets. Inset A shows location of study site in Duncan, British Columbia, Canada. Inset B shows the boresight calibration ground control point setup. (For interpretation of the references to color in this figure legend, the reader is referred to the web version of this article.)

The workflow used to generate radiance and surface reflectance orthorectified images integrates three software modules unique to the manufacturer's systems (HySpex AIR, HySpex NAV and HySpex RAD) with three system independent commercial software packages (PosPac, PARGE and ATCOR-4).The overall data processing for Hyspex HSI can be found in Koirala et al. (2017). The HySpex AIR module captures the data in a raw format. The HySpex RAD module converts the raw data to at-sensor radiance in units of W/m2 sr nm. POSPac (Applanix, Richmond Hill, ON, Canada), is used to process the INS data to extract position and attitude at 200 Hz, as well as the GPS times for all the events. The HySpex NAV module utilizes the output from POSPac to generate INS data for each frame of the flight lines. PARGE utilizes the output from the NAV module to georeference and orthorectify the at-sensor radiance imagery (nearest neighbour interpolation to retain spectral fidelity) using the high-resolution DSM, sensor model, boresight offsets and INS file as inputs., PARGE merges the separate VNIR and SWIR flight lines into single full-range images and generates mosaics. ATCOR-4 is used for atmospheric compensation.

2.4. Atmospheric compensation

The conversion from the orthorectified at-sensor radiance imagery to surface reflectance was undertaken using either a radiation transfer model atmospheric compensation or an empirical line correction depending on illumination conditions. For the SUN imagery (direct illumination conditions, Fig. 4a, Supplementary Video 4), ATCOR-4, an atmospheric compensation software based on the MODTRAN®-5 radiation transfer code was used. ATCOR-4 has been shown to generate accurate surface reflectance imagery from a range of hyperspectral sensors (e.g. Black et al., 2014; Giardino et al., 2015; Markelin et al., 2017; Richter and Schläpfer, 2002) including low altitude UAV data (e.g. Aasen et al., 2018; Arroyo-Mora et al., 2019). The SUN imagery was processed to surface reflectance based on the sensor laboratory calibration information and physical modeling of the irradiance conditions with the parameters in Table 3. The parameters were chosen based on recommended settings for MODTRAN taking into account the latitude, average air temperature of the site and proximity to urban centers (Manolakis et al., 2016).

Terrain-dependent illumination correction is not applicable to this high spatial resolution UAV imagery due to the high variations of irradiance at the leaf level, which cannot currently be parameterized (Richter and Schlapfer, 2019). Small spectral shifts are common to high spectral resolution UAV hyperspectral instruments. Therefore, a spectral recalibration was performed based on atmospheric absorption features (Richter et al., 2011). This processing was purely model based (i.e. no reference panel targets were used for data recalibration).

Currently, physical inversion based on radiative transfer models alone is not feasible for scenes acquired under cloudy or variable conditions (Richter and Schlapfer, 2019; Wright et al., 2020). For the DIFF and VAR imagery (Fig. 4B, Supplementary Video 4), an empirical line correction (ELM) (Smith and Milton, 1999) was carried out using two reference panels (10% Permaflect™ and 50% Spectralon™). Because the field measurements of the reference panels showed considerable in-scattering from nearby vegetation (see results, Section 3), laboratory reflectance spectra of these panels were used instead of the in-situ acquired panel spectra. The panels had been characterized in the lab following field deployment with estimated absolute reflectance following (Elmer et al., 2020; Soffer et al., 2019). Estimated absolute

Fig. 2. Example of the reference panel setup at CGOP in support of UAV-HSI acquisition. The tripod with the SPN1 and camera with fisheye lens can be seen in the background. The tripod system used for the ASD spectroradiometer is implemented specifically to avoid operator influences on the measurements and to maintain consistent viewing conditions to mitigate the complications due to the spectral and angular properties of reference panels (Elmer et al., 2020; Soffer, 2014).

Table 2
Summary of the main specifications of the Mjolnir VS-620 used for the UAV-HSI acquisition.

	V-1240	S-620
Spectral range	400–1000 nm	970–2500 nm
Combined spectral range	400–2500 nm	
Spatial pixels	1240	620
Combined spatial pixels	620	
Spectral channels and sampling interval	200 bands @ 3.0 nm	300 bands @ 5.1 nm
Combined spectral channels	490	
F-number	f1.8	f1.9
FOV	20°	20°
Combined FOV	20°	
IFOV across/along track	0.27 /0.54 mrad	0.54 /0.54 mrad
Bit resolution	12 bits	16 bits
Noise floor	2.37 e^-	80 e^-
Dynamic range	4400	10,000
Peak SNR (at full resolution)	> 180:1	> 900:1
Max speed (a full resolution)	285 fps	100 fps
Detector type	Silicone CCD	Mercury Cadmium Telluride (MCT) FPA
Smile and keystone	< 10% per pixel per band	
Radiometric calibration traceability	To a Physikalisch-Technische Bundesanstalt (PTB) standard	
Power consumption*	50 W	
Dimensions (l-w-h)	374–202–178 mm	
Weight*	< 6.5 kg including standard battery	

* Includes INS and DAU.

reflectance is independent of illumination intensity or conditions. An independent laboratory assessment of their uniformity indicates that all panels are within 0.02–0.2% deviation from the reflectance of the center point across the 400-2500 nm range.

Because diffuse illumination conditions are relatively homogenous across the small area covered by the flight lines (Fig. 1, Table 1) no direct reflection processes are contributing to the adjacency effects. It is therefore possible to assume a fairly constant adjacency effect across the image. This same effect also reduces the impact of BRDF effects on the panel reflectance accuracy. In the field, the panels are used under a hemispherical-directional illumination-viewing geometry (Milton et al., 2009; Nicodemus et al., 1977) that reduces the bidirectional effects especially from the illumination side, whereas on the observation side, the observation zenith angle is close to nadir and as such is comparable to laboratory measurements.

In both cases (radiative transfer model and ELM) the spectral range of the fully absorbing water vapor bands at 1400 and 1900 nm and above 2450 nm where minimal radiance is recorded were omitted for spectral evaluation. A spectral polishing filter (Savitzky Golay filter) with a factor of 5 was applied to smooth small-scale spectral variations.

2.5. Data analysis

2.5.1. Illumination conditions

To characterize the sky conditions from the SPN1, the total, direct and diffuse irradiance were extracted for each entire day as well as for

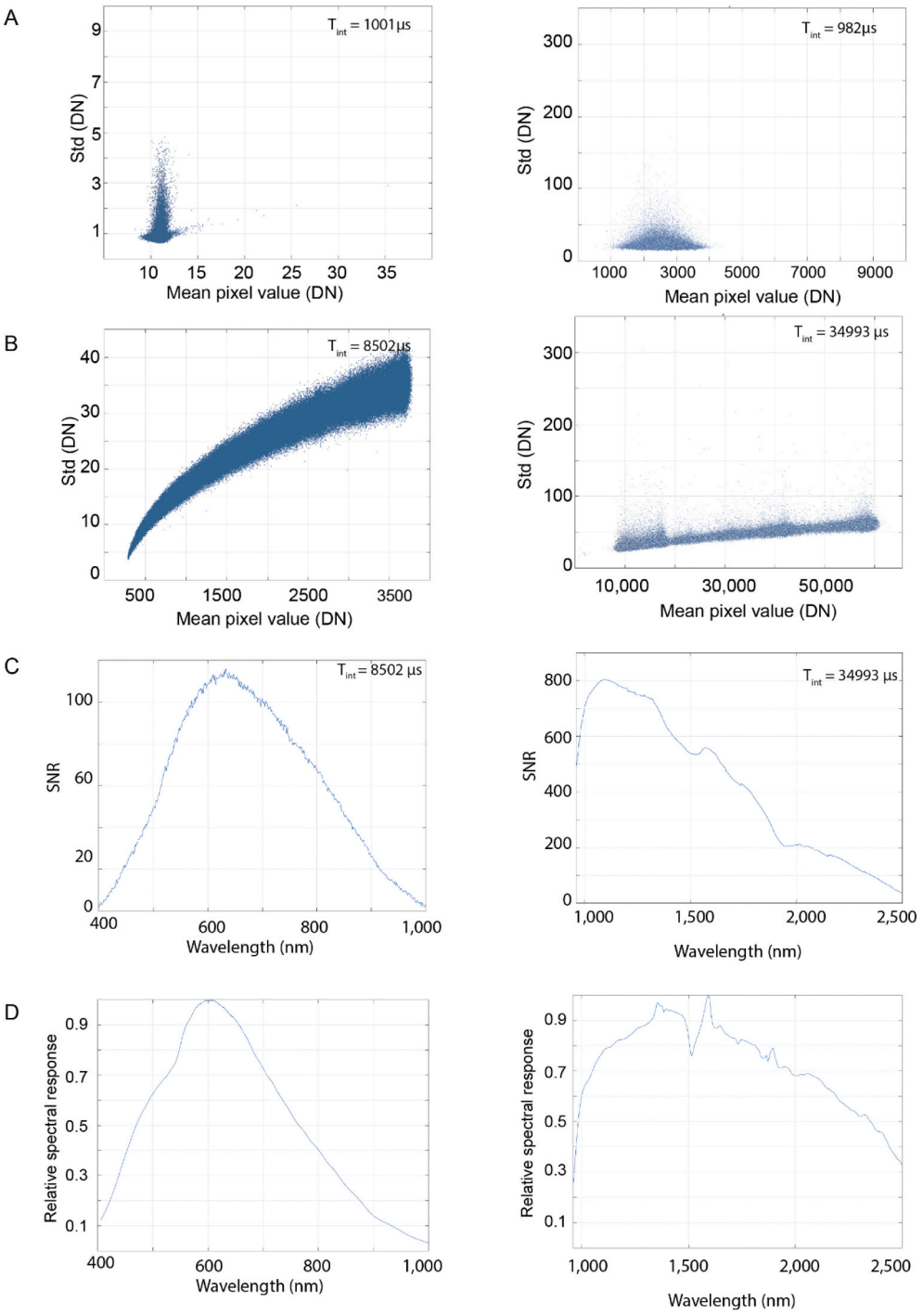

Fig. 3. Dark current determined noise floor from an integration time of 1001 µs for the V-1240 and 982 µs for the S-620 (A) and photon noise (B), determined from a Laboratory integrating sphere using integration times of 8.5 ms for the V-1240 and 33.99 ms for the S-620. Native pixel SNR by wavelength (C) for both sensors. For the V-1240 there are 1392 (native spatial) x 488 (native spectral) pixels that are written to disk. These are resampled and binned to make a 1240 (spatial) x 200 (spectral) product. For the final imagery which is merged with the S-620, the spatial pixels are binned off chip (in software) to produce 620 pixels across track. This results in an increase by a factor of 3.3 in SNR according to: $(1392*488*2/620/200)^{0.5} = 3.3$. For the S-620 imagery there are 640 (native spatial) x 460 (native spectral) pixels. These are resampled to produce an image with 620 spatial × 300 spectral pixels. Accordingly, in the final image product there is an increase in the SNR by a factor of 1.6 according to: $(640*460/620/300)^{0.5} = 1.6$. The SNR shown in (C) is prior to any binning, therefore the factors of 3.3 (VNIR) and 1.6 (SWIR) have not been applied. (D) Spectral response functions of the VNIR and SWIR sensors.

the period of UAV-HSI acquisition. Summary statistics were calculated to describe the variability between dates and a non-parametric Kruskal-Wallis test was applied to examine statistical differences between dates in terms of total, direct and diffuse illumination.

2.5.2. *Surface reflectance spectra*

The in situ spectroradiometer measurements of the reference panels were compared to those collected under laboratory conditions. Similarly, the surface reflectance spectra of the reference panels following the ELM atmospheric compensation were compared to the known reflectance of the panels to assess the quality of the atmospheric compensation under diffuse and variable irradiance conditions.

2.5.3. *Signal to noise ratio (SNR)*

The SNR is the ratio of the signal to the sum of all sources of noise (Giles et al., 1998). From the raw digital number of the HSI detectors, an accurate evaluation of the SNR in every pixel can be calculated. The peak SNR of a system (Table 1) characterizes the full-well of the detector (i.e. number of photoelectrons a photodiode can hold) (Giles et al., 1998; Lambert and Waters, 2014). In contrast, the SNR as a function of wavelength illustrates the efficiency of the system under specific at-sensor radiance conditions and target radiance. Most modern detectors are dominated by photon noise (shot noise), which is due to the random generation of electron-hole pairs in the detector. This noise can be described by a Poisson distribution (Heli, 2006). For the number of

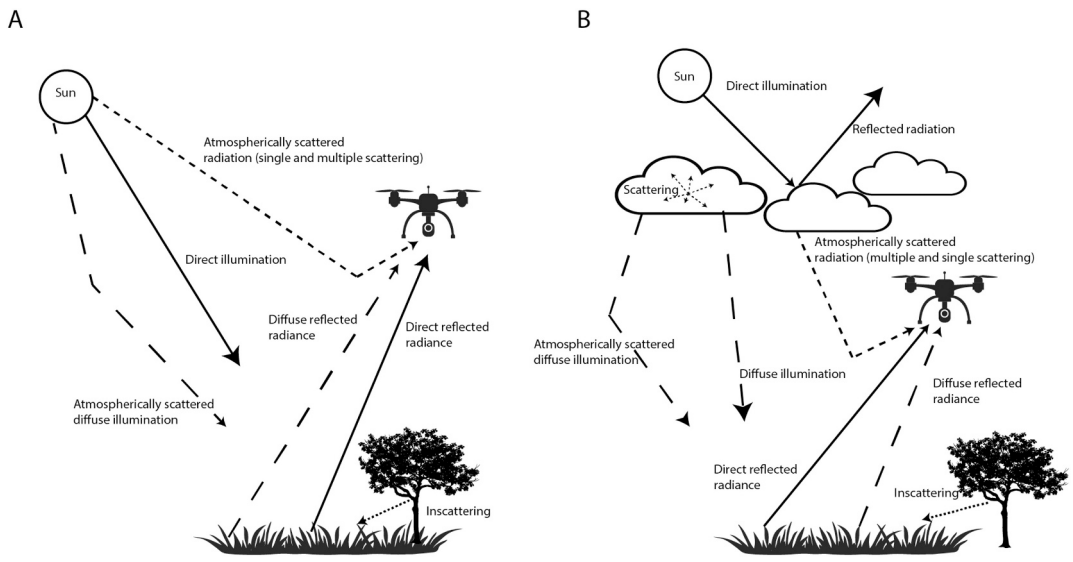

Fig. 4. Main differences to contributions to the at-sensor radiance from various physical processes including direct solar illumination, diffuse atmospheric illumination, and in-scattering that is reflected from the ground/objects to the sensor and scattered radiation that does not interact with the surface (i.e. scattered from atmosphere) on a sunny day (A) versus with cloud cover (B). Low altitude UAV-based sensor is shown acquiring HSI below the cloud deck.

Table 3
Atmospheric compensation parameters applied in ATCOR-4 for the SUN imagery acquired under direct illumination conditions.

Parameter	Value
Model type	Flat terrain
MODTRAN reference atmosphere	Mid-latitude
Aerosol model	Rural
Visibility	60 km
Water vapor absorption band	820 nm

randomly generated electron-hole pairs, N, the SNR can be described as a function in relation to the photon shot noise (Eq. (1)):

$$Noise = \sqrt{N} \tag{1}$$

The SNR as a function of the full-well (FW) and noise floor (N_f) is calculated as Eq. (2):

$$SNR = \frac{FW}{\sqrt{FW + N_f^2}} \tag{2}$$

The number of electrons-hole pairs per digital number (S_f) is a function of the full-well and the radiometric resolution (Res) in analog-to-digital units (ADU) calculated as (Eq. (3)):

$$S_f = {FW}/{Res} \tag{3}$$

During calculation of the at-sensor radiance, the dark current is subtracted from the raw signal; for MCT detectors the dark current can be high and can contain some noise. Dark current is the creation of electron-hole pairs from the system itself rather than exposure to an incident photon (i.e. signal) (Giles et al., 1998). Dark current is influenced by temperature and therefore, detectors, especially in the SWIR need to be cooled in order to minimize it. The photon noise can also have a large contribution to the dark current due to thermally excited electron-hole pairs. The total noise in the dark current is also dependent on how many frames of dark current (DF) have been averaged during an acquisition sequence. Therefore, the total noise in the dark current (N_{dark}) for a given digital number (DN) is (Eq. (4)):

$$N_{dark} = \frac{\sqrt{\left(N_f^2 + (DN \cdot S_f)\right)}}{\sqrt{DF}} \tag{4}$$

The total maximum SNR in a single pixel is then given by the raw digital number, DN_{raw}, of the signal and the digital number of the dark current, DN_{dark}, as follows (Eq. (5)):

$$\begin{aligned} SNR_{max} &= \frac{DN_{raw} \cdot S_f - DN_{dark} \cdot S_f}{\sqrt{N_f^2 + (DN_{raw} \cdot S_f) + N_{dark}^2}} \\ &= \frac{DN_{raw} \cdot S_f - DN_{dark} \cdot S_f}{\sqrt{N_f^2 + (DN_{raw} \cdot S_f) + \left(\frac{\sqrt{\left(N_f^2 + (DN_{dark} \cdot S_f)\right)}}{\sqrt{DF}}\right)^2}} \end{aligned} \tag{5}$$

Using the S-620 as an example, N_f, was determined in the laboratory to be 80 electrons (Fig. 3A) (Nicolas and Baarstad, 2019) with a peak SNR for the system of approximately 900 (Table 2, Fig. 3C). From Eq. (2) we estimate a full-well of approximately 810,000 electrons. The detector has a 16-bit radiometric resolution (65,535 ADU) and 200 dark frames were acquired and averaged. Therefore, following Eq. (3), S_f is 12.36. Eq. (6) is an example maximum SNR (SNR_{max}) for a pixel with raw digital number of 30,000 DN and a dark current of 10,000 DN:

$$\begin{aligned} SNR_{max} &= \frac{30000 \cdot 12.36 - 10000 \cdot 12.36}{\sqrt{80^2 + (30000 \cdot 12.36) + \left(\frac{\sqrt{\left(80^2 + (10000 \cdot 12.36)\right)}}{\sqrt{200}}\right)}} \\ &= \frac{247800}{\sqrt{80^2 + (371400) + 25.5^2}} \approx 403 \end{aligned} \tag{6}$$

Eq. (5) was applied to the flight lines (V-1240 and S-620 separately) for all three dates. Pixels of SNR_{max} representing tree canopies and herbaceous vegetation were extracted by generating a random sample and adjusting sample locations that were located in areas outside the classes of interest. For the SUN image a direct shadow class cast by the trees onto the herbaceous vegetation was also included. A total of 41,000–156,000 pixels per class were extracted for all three dates. Best-fit probability density functions based on the Akaike Information Criterion (AIC) were calculated to compare the distributions of SNR_{max} across varying illumination conditions. The mean SNR of all pixels for all

wavelengths was also determined for each date.

2.5.4. Spectral vegetation indices

In order to assess the potential impact of variable illumination conditions on spectral vegetation indices (SVIs) of canopy leaves and herbaceous vegetation, three SVIs from the VNIR region and three from the SWIR region were calculated (Table 4). The selected SVIs in the VNIR are related to leaf pigments such as chlorophyll, carotenoids and anthocyanins, and have been commonly use in vegetation studies from different latitudes (Beamish et al., 2018; Gamon et al., 1995; Gitelson et al., 2001). SVIs using the SWIR region were selected to cover a wide range of biochemical constituents such as cellulose, lignin and water, which are important for vegetation stress studies and non-photosynthetic vegetation determination (Gao, 1996; Nagler et al., 2003; Serrano et al., 2002). Based on the proportion of canopy and herbaceous vegetation within each mosaic (estimated from the DSM) we selected 20–50 9 × 9 cm pixel windows (1200–1500 pixels per class per date) to calculate the SVIs and relate them to the direct and diffuse illumination conditions. Differences between SVIs from different illumination conditions and classes were compared based on a non-parametric ANOVA (Kruskal-Wallis test) with a Dunn's multiple comparison test.

2.5.5. Endmember identification

Endmembers are commonly used to identify multiple constituent materials within mixed pixels. A spectral endmember is a theoretical representation of the spectral albedo (i.e. the bi-hemispherical reflectance) of a pure material within a scene. Often, the nadir reflectance at the time of data acquisition of a material is taken alternatively as an endmember. Mapped in *n*-dimensional space, mixtures of endmembers fall within a simplex formed with the pure materials at the vertices and therefore, regardless of the dimensions of the data (i.e. number of bands), the dimensionality of the HSI is the number of distinct materials in the scene (Eismann, 2012). Because endmembers can represent not only pure 'materials' but also both environmental/biophysical variations (e.g. different pigment concentrations) and illumination (and atmospheric) induced differences, endmember identification can reveal differences in the proportional contribution of environmental versus illumination/atmospheric origins within the scene (Gruninger et al., 2004) as a result of irradiance conditions. For two dates with different illumination conditions (i.e. high direct irradiance and high diffuse irradiance) the Sequential Maximum Angle Convex Cone (SMACC) endmember model was used to extract the most distinct spectral endmembers in the atmospherically corrected mosaics (SUN and DIFF, respectively). This algorithm locates endmembers that account for environmental and biophysical conditions representing the spectral variability of the materials in the scene as well as illumination effects which often can be seen as extreme spectra (Gruninger et al., 2004). A positivity constraint was used (i.e. the abundance images cannot contain negative values). The first endmember identified by SMACC is the spectrum from the brightest pixel in the image, followed by the one that is most different (Gruninger et al., 2004). It iteratively adds the most different spectrum from those included in the set. An assumption for SMACC is that each pixel contains a high percentage of a single material with unique combinations of others. In this case, 'material' does not only correspond to physical materials (e.g. flowers, leaves from an herbaceous species) or biophysical differences, but can include endmembers that are due to illumination conditions as well.

Table 4
Narrowband spectral vegetation indices calculated for canopy and herbaceous vegetation for the three sampling dates. ρ represents reflectance at the given wavelength (in nm).

Index	Formula	Reference
Normalized Difference Vegetation Index (NDVI)	$\frac{\rho 750 - \rho 680}{\rho 750 + \rho 680}$	Rouse Jr. et al., 1974
Carotenoid Reflectance Index 1 (CRI1)	$\frac{1}{\rho 510} - \frac{1}{\rho 550}$	Gitleson et al., 2002
Anthocyanin Reflectance Index 2 (ARI2)	$\rho 800 \times \left(\frac{1}{\rho 550} - \frac{1}{\rho 700}\right)$	Gitelson et al., 2001
Cellulose Absorption Index (CAI)	$0.5 \times \left(\frac{\rho 2000 - \rho 2200}{\rho 2100}\right)$	Nagler et al., 2003
Normalized Difference Lignin Index (NDLI)	$\frac{log\frac{1}{\rho 1754} - log\frac{1}{\rho 1680}}{log\frac{1}{\rho 1754} + log\frac{1}{\rho 1680}}$	Serrano et al., 2002
Normalized Difference Water Index (NDWI)	$\frac{\rho 860 - \rho 1240}{\rho 860 + \rho 1240}$	Gao, 1996

3. Results

3.1. Illumination characterization

Downwelling irradiance results from the SPN1 pyranometer reveal significant illumination variability as a consequence of different cloud cover conditions for the three data collection dates (Fig. 5, Table 5, Supplementary Video 4). As expected, the highest values of total and direct irradiance were recorded during clear sky conditions (Fig. 5A). Results from the $9^{1/2}$-min-long UAV-HSI acquisition, reveal homogeneous illumination conditions (i.e. low standard deviation), where total irradiance ranged from 785.7 $W{\cdot}m^{-2}$ to 850.7 $W{\cdot}m^{-2}$ ($\bar{x}_{\text{Tot-SUN}}$ = 852.4.5 $W{\cdot}m^{-2}$, $\sigma_{\text{Tot-SUN}}$ = 16.38 $W{\cdot}m^{-2}$), direct irradiance ranged from 574.4 $W{\cdot}m^{-2}$ to 646.6 $W{\cdot}m^{-2}$ ($\bar{x}_{\text{Dir-SUN}}$ = 624.6 $W{\cdot}m^{-2}$, $\sigma_{\text{Dir-SUN}}$ = 16.63 $W{\cdot}m^{-2}$), and diffuse irradiance ranged from 190.3 $W{\cdot}m^{-2}$ to 223.3 $W{\cdot}m^{-2}$ ($\bar{x}_{\text{Dif-SUN}}$ = 200.8 $W{\cdot}m^{-2}$, $\sigma_{\text{Dif-SUN}}$ = 9.4 $W{\cdot}m^{-2}$) (Fig. 5A, Table 5). DIFF measurements were taken under overcast conditions and for the $9^{1/2}$-min-long UAV-HSI acquisition (Fig. 5B, Supplementary Video 4). Thus, DIFF measurements show total irradiance ranged from 191.3 $W{\cdot}m^{-2}$ to 241.1 $W{\cdot}m^{-2}$ ($\bar{x}_{\text{Tot-DIFF}}$ = 217.1 $W{\cdot}m^{-2}$, $\sigma_{\text{Tot-DIFF}}$ = 16.79 $W{\cdot}m^{-2}$), with very low direct irradiance ranging from 0.8 $W{\cdot}m^{-2}$ to 4.6 $W{\cdot}m^{-2}$ ($\bar{x}_{\text{Dir-DIFF}}$ = 2.5 $W{\cdot}m^{-2}$, $\sigma_{\text{Dir-DIFF}}$ = 0.9 $W{\cdot}m^{-2}$), with a higher diffuse component than for SUN (min $_{\text{Dif-DIFF}}$ = 189.8 $W{\cdot}m^{-2}$, max $_{\text{Dif-DIFF}}$ = 239.2 $W{\cdot}m^{-2}$, $\bar{x}_{\text{Dif-DIFF}}$ = 214.6 $W{\cdot}m^{-2}$, $\sigma_{\text{Dif-DIFF}}$ = 16.61 $W{\cdot}m^{-2}$). Finally, irradiance VAR measurements (Fig. 5C), reveal larger range values in SUN or VAR (Range $_{\text{Tot-VAR}}$ = 118.2 $W{\cdot}m^{-2}$, Range $_{\text{Dir-VAR}}$ = 109.8 $W{\cdot}m^{-2}$ and Range $_{\text{Dif-VAR}}$ = 79.4 $W{\cdot}m^{-2}$) (Table 5).

Results from the Kruskal-Wallis non-parametric test show a significant difference ($p < 0.0001$) for total (n = 186, H = 135), direct (n = 186, H = 139.7) and diffuse (n = 186, H = 37.97) irradiances across the various illumination conditions. However, the multiple comparison test (Dunn's test) revealed significant differences for total, direct and diffuse irradiances between SUN vs DIFF measurements, and SUN vs VAR, but no significant difference was found between DIFF and VAR (Table 6).

3.2. Reference panels

As expected, reference panels measured in the field near-coincidentally with the UAV-HSI, differ from their laboratory characterization (Fig. 6). The three darkest panels (2%, 10%, 18%) exhibit strong in-scattering from nearby vegetation for SUN measurements (high direct illumination, Fig. 5A-B). In contrast, the 50% panel is more consistent in the VNIR range across the three dates with its laboratory characterization. Its in-situ measured spectrum also has in-scattering effects from the vegetation but are less apparent than in the darker panels. We refer to these results as 'apparent reflectance' from here-on because the 2–5 min required to complete a measurement sequence (i.e. 99% Spectralon normalization panel measurement followed by acquisition of spectra of each of the four panels) led to the measurements being affected by the variability of irradiance between the normalization step and the panel measurements. The low SWIR reflectance observed in the raw digital count from the 99% panel (Fig. 6E) for DIFF measurements (lowest total and lowest direct irradiance, Figs. 6 and 7) is

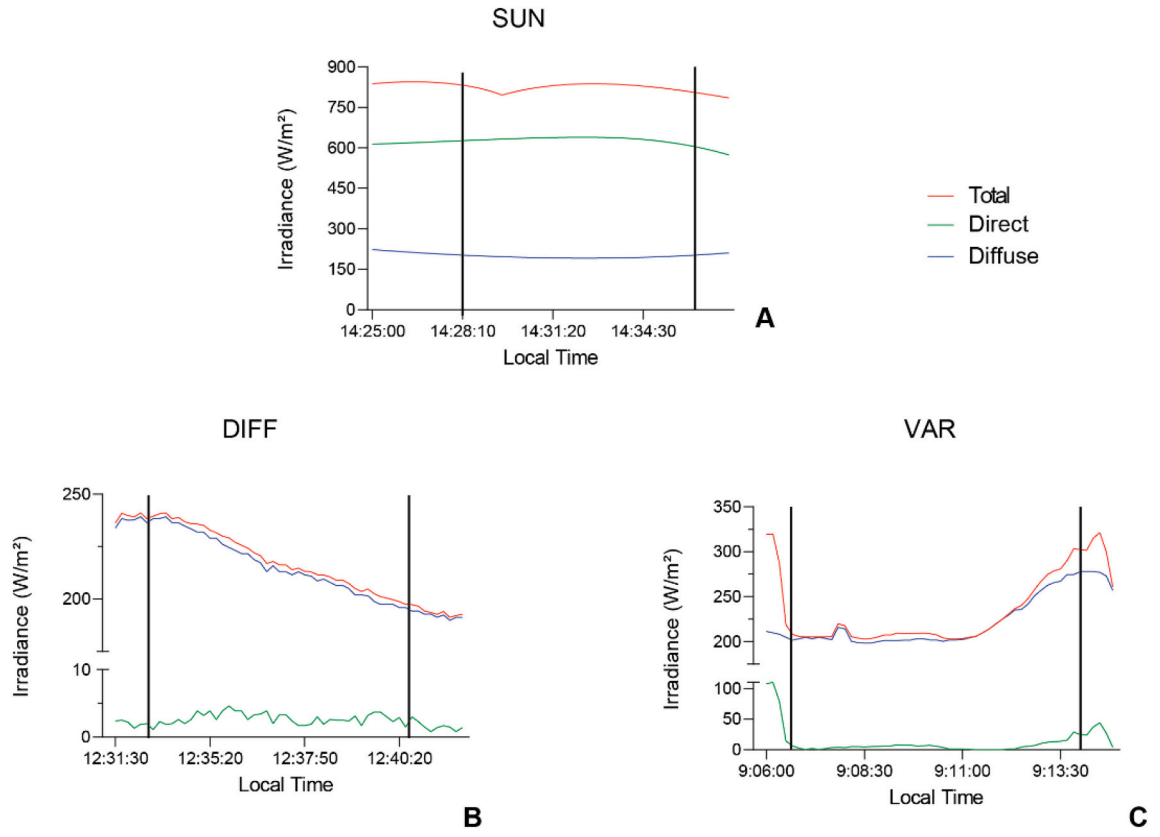

Fig. 5. SPN1 pyranometer profiles the time period where HSI was acquired for three different illumination conditions, SUN (A), DIFF (B) and VAR (C). Vertical lines designate the effective image acquisition outside of transit to and from the takeoff/landing area.

Table 5
Total, direct and diffuse irradiance ($W \cdot m^{-2}$) measured with the SPN1 pyranometer for the three sampling days (UAV-HSI flight).

	Total	Direct	Diffuse	Total	Direct	Diffuse	Total	Direct	Diffuse
Minimum	785.7	574.4	190.3	191.3	0.8	189.8	203	0	198.4
Maximum	850.7	646.6	223.3	241.1	4.6	239.2	321.2	109.8	277.8
Range	65.0	72.2	33.0	49.8	3.8	49.4	118.2	109.8	79.4
Mean	825.4	624.6	200.8	217.1	2.5	214.6	235.6	13.0	222.6
Std. deviation	16.38	16.63	9.4	16.79	0.9	16.61	39.96	23.22	28.22

Table 6
Dunn's multiple comparisons test for direct, total and diffuse irradiances across dates.

Total	Mean rank diff.
SUN vs. DIFF*	97.83
SUN vs. VAR*	87.99
DIFF vs. VAR	−9.840
Direct	
SUN vs. DIFF*	104.9
SUN vs. VAR*	80.67
DIFF vs. VAR	−24.23
Diffuse	
SUN vs. DIFF*	−44.41
SUN vs. VAR*	−53.61
DIFF vs. VAR	−9.203

* Difference is significant ($p < 0.05$).

indicative of the cloudy conditions under which most irradiance in the SWIR wavelengths is attenuated. The low irradiance in the SWIR for DIFF is also reflected in the substantial noise of the apparent reflectance spectra of the panels, especially from those with low reflectance (2%, 10%). For the 2% panel all three dates exhibit prominent contamination from vegetation in-scattering, however this effect decreases under cloudy conditions with the panels of higher reflectance (i.e. 10% to 50%). As described in Section 2.5, the variability in irradiance over a measurement sequence, in-scattering and high noise in the SWIR under cloudy conditions precluded the use of these in-situ measured panel data in the atmospheric compensation (ELM applied for DIFF and VAR images).

Comparison of the reflectance of the reference panels extracted from the imagery against the laboratory derived spectra of the panels (Fig. 7) indicates consistency in shape and amplitude (i.e. brightness) for the 10%, 18% and 50% panels for both SUN and VAR (< 5% deviation outside of the noise in the SWIR). For the 2% panel the vegetation in-scattering results in a deviation from the pseudo-invariant feature spectrum expected of the reference panel. The considerable noise in the SWIR due to low irradiance under diffuse conditions (Fig. 4B) can be seen in the image panel spectra (Fig. 7A and C) from DIFF, specifically for the 2% panel that noise extends to the 1500–1700 nm range in addition to the >2000 nm range. It is also notable in the low reflectance targets (2% and 10%) from VAR show a lower magnitude in the two brighter panels (18% and 50%). Despite the noise in the SWIR range in the 10% and 18% panels, the absorption feature around 2300 nm of the Permaflect (10%) and Flexispec (18%) panels can be readily seen from

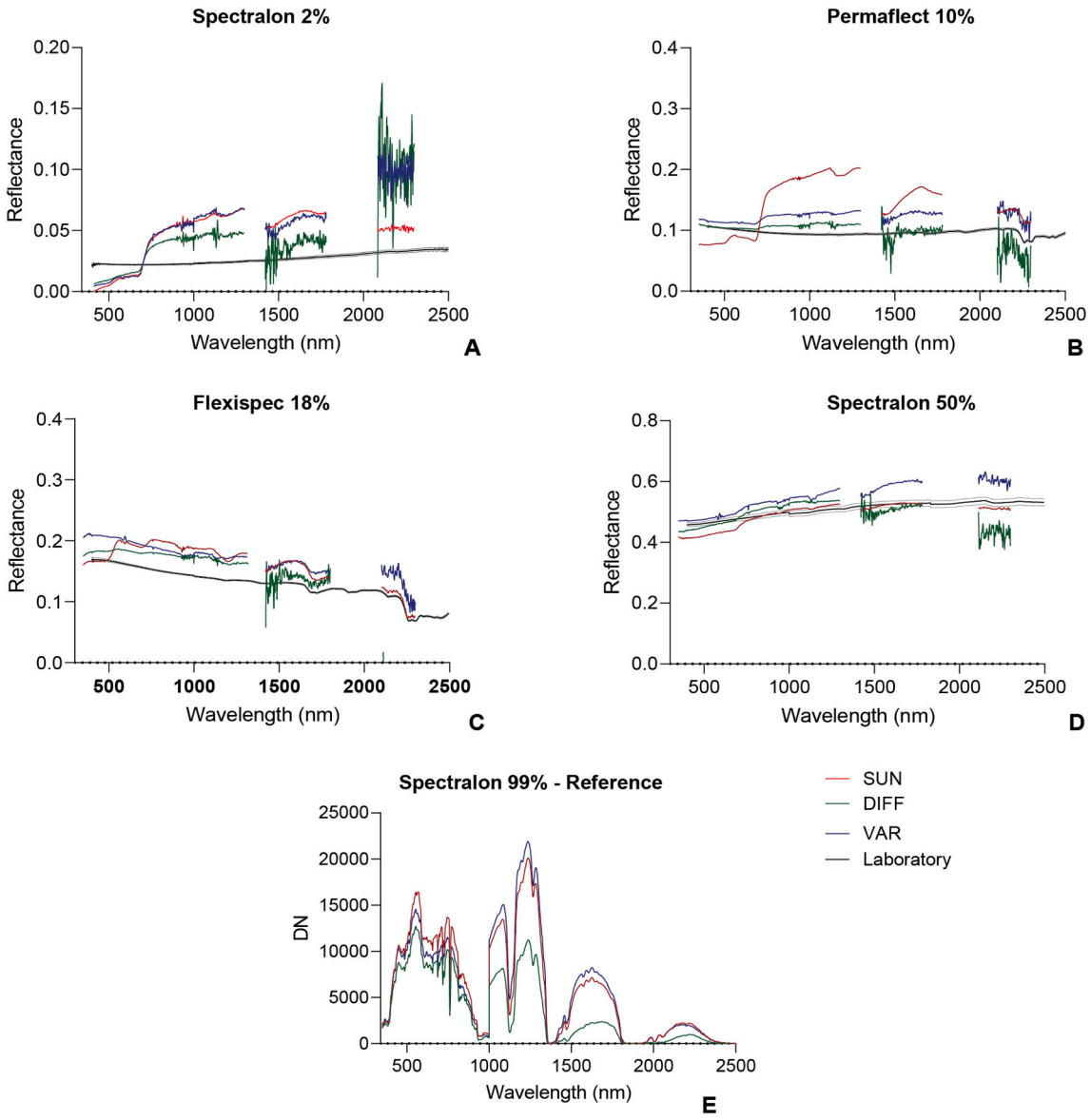

Fig. 6. Comparison of the apparent reflectance of the reference targets across dates as measured in-situ with the spectroradiometer and the UAV-HSI (A, B, C, D). In-situ measurements were done near-coincidentally with UAV-HSI acquisition. E shows digital number (DN) raw values from the 99% Spectralon™ reference panel. Notable contamination from in-scattering from vegetation can be seen in the panel spectra in figures A-D.

the pixel spectra (Fig. 7).

Representative canopy leaf and herbaceous vegetation pixel spectra for the three dates illustrate the impact of the illumination conditions (Fig. 8). Under high direct illumination (Fig. 5A) the increased amplitude of the reflectance across the full spectral range can be seen (Fig. 8). In addition, a residual O_2 band at 760 nm, which is incorrectly accounted for, is indicative of small pixel radiative transfer model based atmospheric compensation resulting in an anomaly within the SUN spectra (high direct illumination), but is not apparent in the two mosaics acquired under diffuse illumination corrected with the ELM. Despite overall magnitude differences being greater in the NIR and SWIR, the inset illustrates differences also in the visible wavelengths (< 700 nm) (Fig. 8). Importantly, the chlorophyll absorption feature in the red is more clearly defined from the imagery collected under direct illumination (SUN). Spatially across the flight lines (Fig. 9), the ELM atmospheric compensation normalized the differences in brightness due to temporal variation in irradiance (DIFF and VAR). Similarly, minor differences in brightness between flight lines from SUN were also minimized through the radiative transfer model atmospheric compensation. The low SNR in the SWIR can also clearly be seen in the imagery from DIFF in comparison to the other two dates.

3.3. SNR

The overall shape of SNR by wavelength resembles the spectral radiance of vegetated pixels (Fig. 10). The average SNR of the raw pixels across all dates illustrates the wavelength dependent impact of illumination across the VNIR-SWIR range with decreased atmospheric transmission at longer wavelengths (Nann, 1990). The SNR in the SWIR at wavelengths > 2000 nm is the lowest as expected under diffuse illumination (Fig. 5B). Less than 5% apparent transmission under moderate to heavy cloud cover is expected in that wavelength region (Evans and Puckrin, 2003). In the imagery from SUN and VAR conditions, the CO_2 doublet at ~2013–2060 nm can be seen, but this is absent in the low signal from DIFF. The major atmospheric water absorption features centered at 900, 1100, 1400 and 1900 nm are prominent in the imagery from all three illumination conditions. The SNR decreases at 776 nm from 196:1 (high direct irradiance, SUN) to 140:1 and 103:1 on VAR and

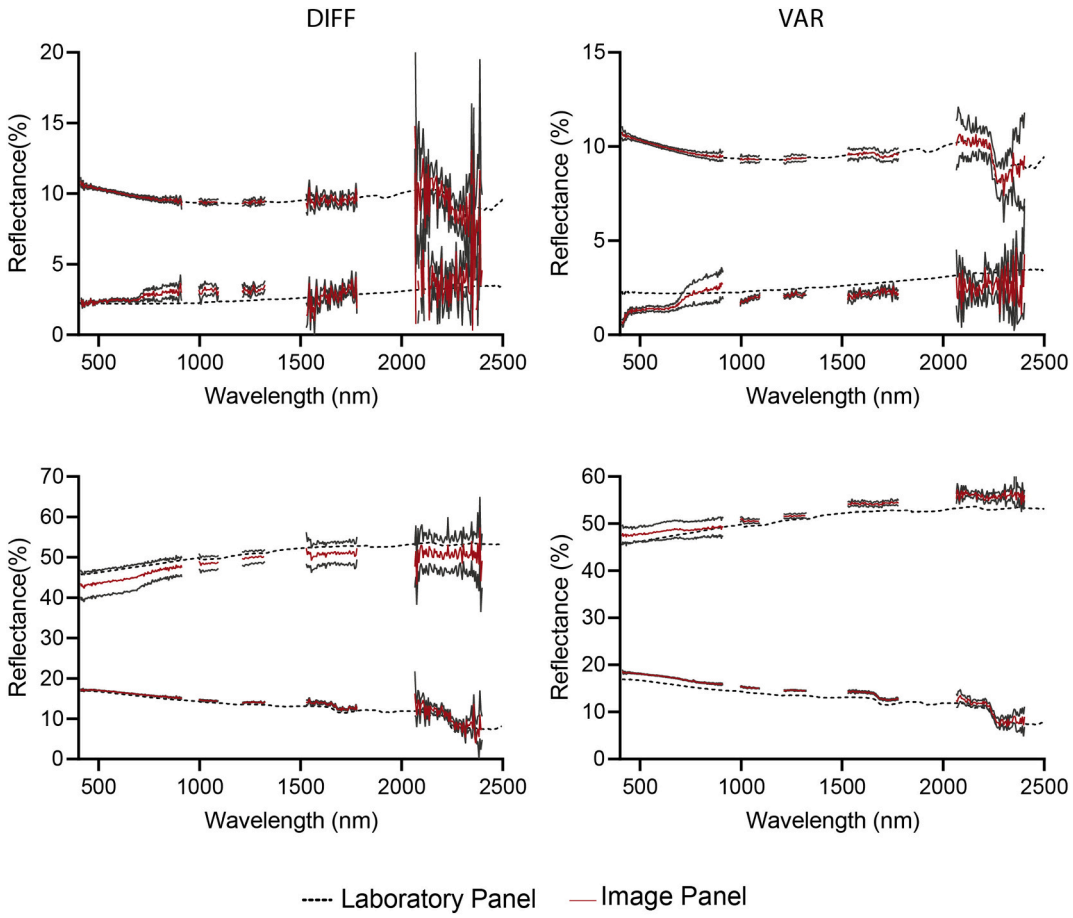

Fig. 7. 2%, 10%, 18% and 50% resampled reference laboratory spectra vs image pixel extracted panel reflectance following atmospheric compensation (ELM method) of the UAV-HSI (DIFF and VAR). Dark gray lines represent one standard deviation for the extracted panel reflectance after atmospheric compensation.

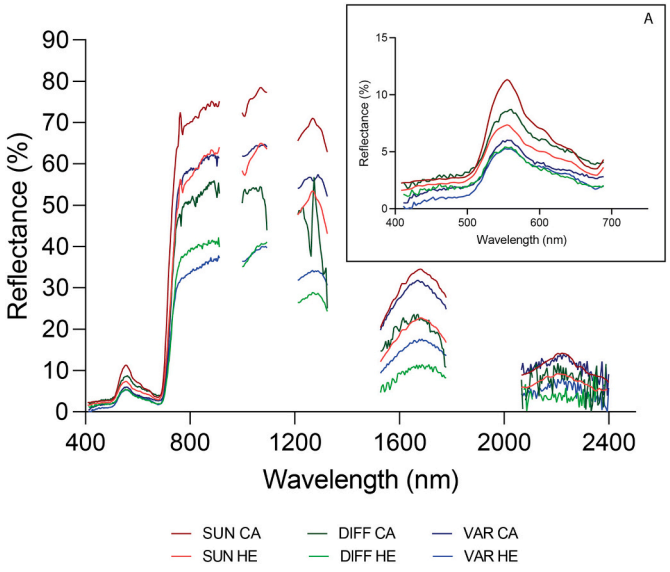

Fig. 8. Canopy (CA) and herbaceous (HE) vegetation spectra comparison across dates following atmospheric compensation of the UAV-HSI. Inset A shows spectra between 400 and 690 nm.

DIFF respectively, indicative of the higher proportion of diffuse irradiance from DIFF measurements (Fig. 5B); the atmosphere is relatively transparent at 776 nm because there is no gaseous absorption and less aerosol scattering, therefore decreases in intensity are attributable to increased cloud cover (Miyauchi, 1985).

When partitioned by vegetation class, SNR_{max} results reveal higher values for both canopy and herbaceous vegetation pixels collected under the highest irradiance conditions (SUN) (Fig. 11). For all illumination conditions, the SNR_{max} of the SWIR exceeds the VNIR (e.g. $\mu_{SUN\text{-}SWIR}$ = 463:1 vs $\mu_{SUN\text{-}VNIR}$ = 200:1 for canopy vegetation under the highest irradiance). It is important to note SNR_{max} represents raw pixel geometry, prior to binning. Only the day with high direct illumination resulted in a distinct shadow class for which the SNR_{max} is comparatively lower. However, for both the VNIR and SWIR, the shadow class has a higher SNR_{max} ($\mu_{SUN\text{-}VNIR}$ = 80:1 and $\mu_{SUN\text{-}SWIR}$ = 157:1, respectively) than the herbaceous vegetation class observed under diffuse illumination ($\mu_{DIFF\text{-}VNIR}$ = 73:1 and 53:1 and $\mu_{DIFF\text{-}SWIR}$ = 142:1). Canopy vegetation under diffuse illumination was found to have marginally higher SNR_{max} ($\mu_{DIFF\text{-}VNIR}$ = 74:1 and $\mu_{DIFF\text{-}VNIR}$ = 110:1, and $\mu_{DIFF\text{-}SWIR}$ = 249:1 and $\mu_{DIFF\text{-}SWIR}$ = 210:1 in the SWIR) than shadow pixels under direct illumination. When comparing canopy versus herbaceous vegetation in terms of SNR_{max}, our results reveal consistently higher values of SNR for canopy pixels than for herbaceous pixels in both VNIR and SWIR (Figs. 10, 11).

3.4. Spectral vegetation indices (SVIs)

Fig. 12 shows that the impact of illumination conditions on SVIs is index dependant. Across dates, NDVI is significantly higher ($p < 0.0001$) for canopy pixels than for herbaceous vegetation (Table 7, Fig. 12A). For both classes, we found non-significant difference in NDVI between SUN and VAR despite a significant difference in total illumination between

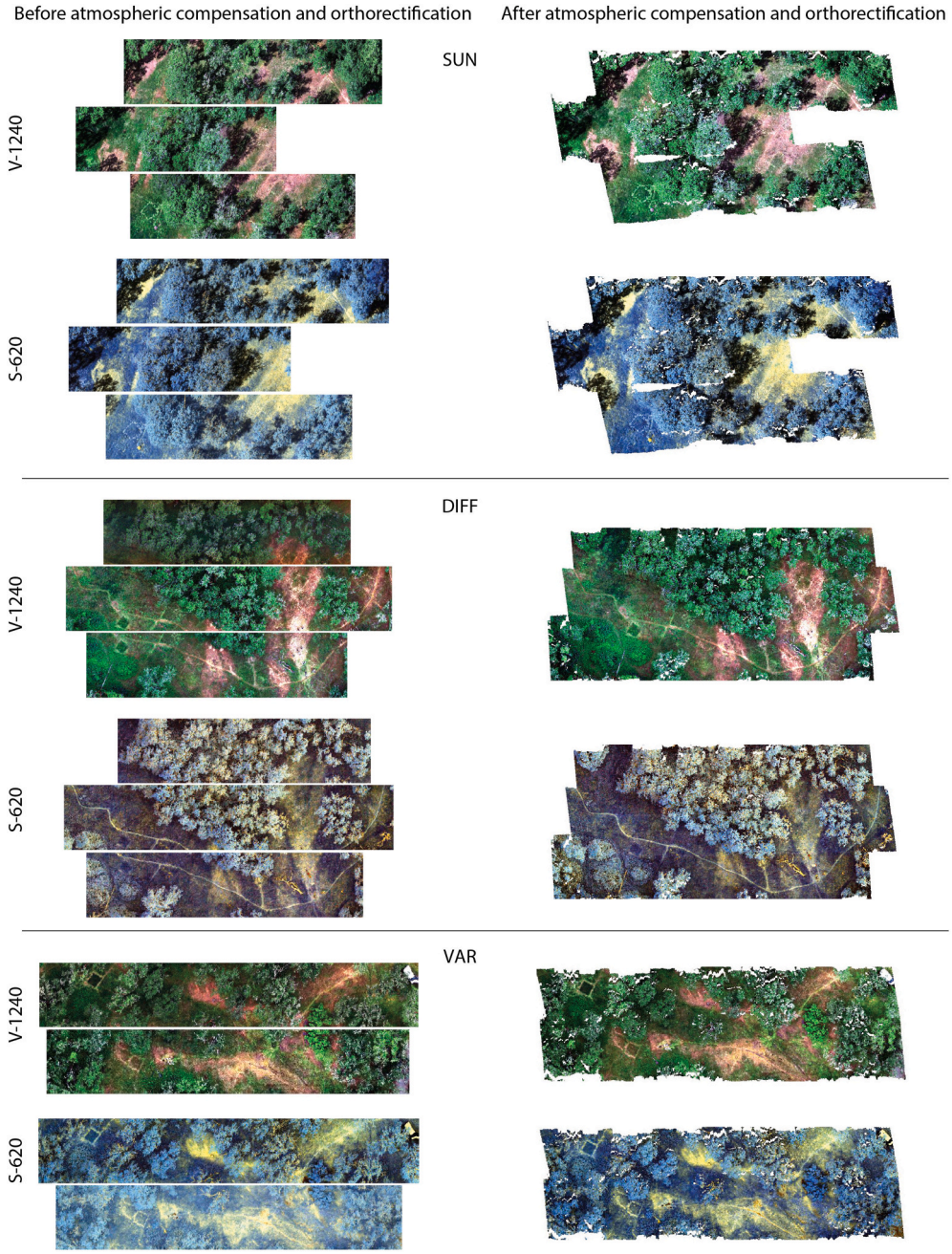

Fig. 9. Illustration of the UAV-HSI as separate VNIR and SWIR flight lines as non-geocorrected radiance (left) and orthorectified reflectance following atmospheric compensation (right). VNIR imagery is shown as R: 632 nm G: 542 nm B: 454 nm. SWIR imagery is shown as R: 2192 nm G: 1614 nm B: 1246 nm. All lines have been enhanced with a linear 2% stretch. The average pixel size of the non-geocorrected flight lines is approximately 1 cm, and the resampled pixel size for the geocorrected mosaics is 3 cm.

those dates (Table 6). However, in comparison to DIFF measurements (highest diffuse irradiance with negligible direct irradiance), we found significant differences in NDVI from SUN and VAR conditions for both classes. For CRI, under highly variable illumination, we found no significant difference between canopy and herbaceous vegetation ($p > 0.99$) (Fig. 12B). For canopy vegetation we found CRI to be sensitive to illumination conditions with significant differences across three dates ($p < 0.0001$), while for herbaceous vegetation we found that SUN and DIFF conditions are not significantly different ($p > 0.99$) (Table 7). For ARI we found significant differences across dates and illumination conditions, with higher ARI values for herbaceous vegetation than canopy (Fig. 12C). Also, across illumination conditions, ARI was found to be non-significantly different for canopy pixels collected under predominantly diffuse irradiance (DIFF) and variable irradiance (VAR), as well as for herbaceous vegetation between direct (SUN) and diffuse conditions (DIFF). Despite the apparent overlap between canopy and herbaceous CAI values (Fig. 12D), they are significantly different across classes as well as illumination conditions ($p < 0.0001$) (Table 7), which can be explained by the spatial variability of CAI in the herbaceous class, and in both classes under diffuse illumination (DIFF). NDWI is different between canopy and herbaceous vegetation across all three dates (Fig. 12E), however, under diffuse illumination (DIFF), herbaceous vegetation has the greatest difference in values ($\bar{x} = 0.11$) than the canopy ($\bar{x} = 0.06$) (Table 7). Finally, NDLI shows significant differences between canopy and herbaceous vegetation across illumination conditions ($p < 0.0001$), but non-significant differences within canopy and within herbaceous vegetation under direct illumination (SUN) and variable illumination (VAR) ($p = 0.932$ and $p > 0.99$, respectively).

3.5. Endmember extraction

The endmember extraction results for the two contrasting

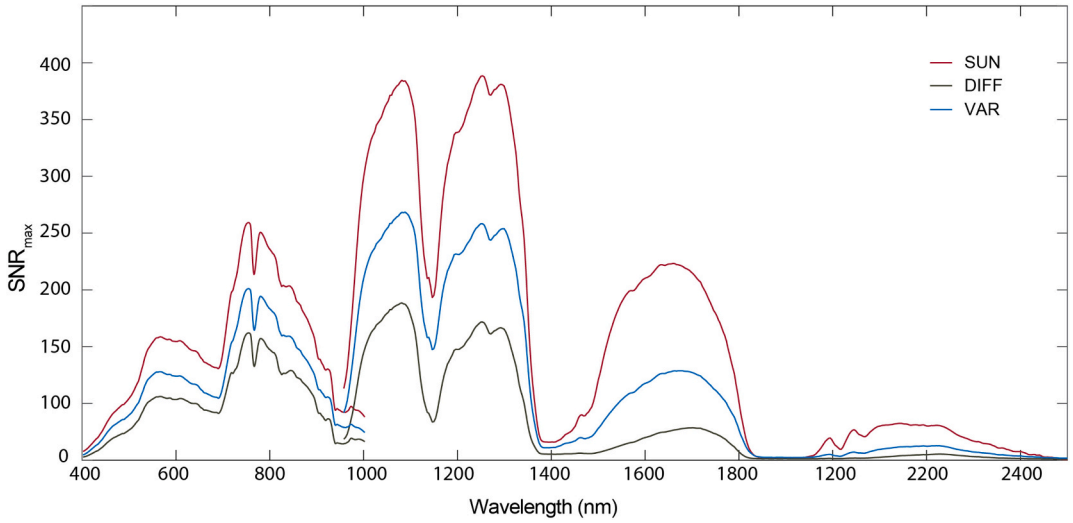

Fig. 10. Average maximum SNR (SNR_{max}) of the raw images across dates.

illumination conditions (predominantly direct illumination – SUN, versus predominantly diffuse illumination – DIFF) highlight different components of the scene (Fig. 13). With predominantly direct illumination, the endmember with the highest abundance highlights the directionality of the illumination (solar azimuth = 212.7°) with sunlit and shadowed sides of the tree canopies clearly differentiated. The abundance of the "green vegetation" endmember incorrectly varies with canopy position with values >0.75 on the side of the canopy facing the illumination versus values <0.6 on the opposite side. In addition to the shadow specific endmember, three of the main endmembers are specific to pixels within the shadowed components of the mosaic differentiating gradations from the umbra to the penumbra. An additional three endmembers extract various aspects of the non-photosynthetic components of the vegetation, mosses and lichens visible on the branches. Only one endmember is specific to the herbaceous vegetation of the meadow. In contrast, under diffuse illumination, five of the most predominant endmembers separate components of the meadow herbaceous vegetation and two are specific to the non-photosynthetic vegetation components (Fig. 13). The abundance of the non-photosynthetic components, mosses and lichens are greater (0.40–0.83) than under direct illumination (maximum abundance of 0.2) despite those pixels being entirely composed of those materials. The dominant 'green leaf' endmember illustrates an even illumination of the canopy without BRDF effects. Furthermore, there no differentiation between gradations of shadow as seen on the SUN conditions.

4. Discussion

We demonstrate that atmospherically corrected low altitude UAV-HSI acquired under cloudy conditions (Supplementary Video 4) is useful for vegetation analyses as long as the unique challenges imposed by the illumination conditions are considered. Users must be aware of how such conditions increase the dynamic illumination variation (Wendel and Underwood, 2017) and importantly, their effects on the HSI products.

4.1. Illumination conditions

Downwelling irradiance measurements from the pyranometer ranged from predominantly collimated direct illumination (SUN: 825.4 W/m^2 total irradiance of which 76% was direct), to predominantly diffuse skylight and very low direct irradiance (DIFF: 214.6 and 2.5 W/m^2, respectively). Cloud Optical Depth (τ) and Cloud Particle Size (CPS) (GOES-R Algorithm Working Group and GOES-R Program Office, 2018; Mecikalski et al., 2013; Walther et al., 2013) information from GOES-17 for the duration of the HSI acquisition corroborate, as expected, that for SUN τ was low (1.5–1.8) indicating optically thin clouds (Supplementary Video 4) with a CPS of 36.6–39.7 μm. In contrast, for DIFF, τ was high (6.6–6.7) indicating optically thick clouds (Supplementary Video 4) with a CPS of 42.8–48.3 μm. During the VAR acquisition, τ increased from 1.9 to 3.3 (decrease in CPS from 35.6 to 27.8 μm) indicating a buildup of clouds. The τ determines the quantity of scattering, while CPS is related to the direction of the scattering processes and magnitude of attenuation (Walther et al., 2013); larger liquid water droplets result in greater absorption of irradiance (Heidinger et al., 2018).

For a UAV-HSI platform, stability and speed are very important to minimize attitude induced artifacts (Arroyo-Mora et al., 2019; Freitas et al., 2018). Therefore, our flight plan considered only 2–3 flight lines at a time, at a speed of 1 m/s, which increased the likelihood of changes in dynamic illumination. The changes in illumination can be clearly seen in the differences in brightness between flight lines in the non-geocorrected radiance DIFF and VAR imagery (Fig. 9). Of additional consideration for the SUN image is the potential of irradiance enhancement (Pecenak et al., 2016) which has been shown to be prevalent in spatially and temporally heterogeneous optically thin clouds with substantial forward scattered diffuse irradiance (Supplementary Video 4) (Bartlett et al., 1998; Berg et al., 2011; Pecenak et al., 2016). While likely only a small contribution (< 5–10%) to the total irradiance based on the τ and the solar zenith angle at the time of image acquisition (Table 1), it could explain the overall high total irradiance (825.4 W/m^2) of which 24% are diffuse (Table 5). Importantly, the scattering and attenuation by the water vapor and liquid/ice droplet composition of the clouds is wavelength dependent. The SWIR wavelengths are attenuated the most but the red and NIR wavelengths are also noticeably affected, resulting in a relatively higher intensity of UV and blue wavelengths (Lubin and Vogelmann, 2011; Nann, 1990). An increase in τ from 1 to 5 decreases transmission of light through the clouds by at least an additional ~25% at wavelengths greater than 1000 nm (Lubin and Vogelmann, 2011). For the DIFF imagery (negligible direct illumination = 2.5 W/m^2 Table 5, Fig. 5, Supplementary Video 4), the majority of the downwelling diffuse illumination (214 W/m^2) is likely in the visible wavelengths because of the optically thick cloud clover (τ = 6.6–6.7). Its effect can be seen in the especially low SNR in the SWIR range at wavelengths >1400 nm (Fig. 10). Concurrently, the field spectroradiometer measurements of the 99% Spectralon panel show considerably lower reflected energy in the SWIR (DIFF DN_{2200nm} = 858), compared to the other two conditions, for example, SUN DN_{2200nm} = 2082 and VAR DN_{2200nm} = 1899 (Fig. 6E). The effects of the low irradiance of the

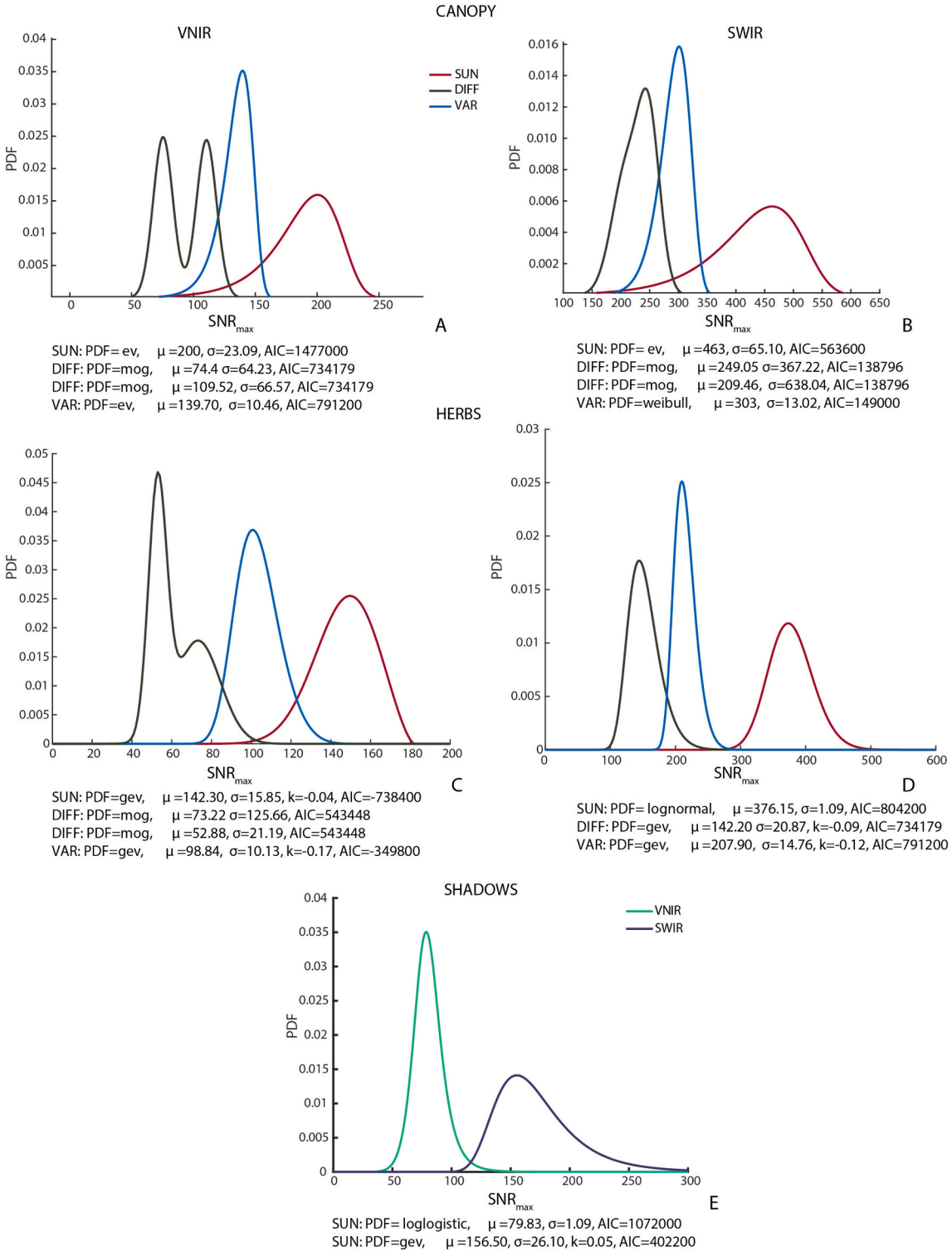

Fig. 11. Probability Density Function (PDF) of maximum SNR (SNR_{max}) for canopy and herbaceous vegetation across dates, for VNIR and SWIR regions. Shadow PDFs for SUN illumination conditions are also included (E).

skylight during the DIFF acquisition can further be seen in the increased noise in the reference panels' apparent reflectance (Fig. 6A-D) acquired both with the spectroradiometer as well as reflectance extracted from the pixels (Fig. 7). The noise due to low SNR is also seen in the reflectance of the canopy leaves and herbaceous vegetation at wavelengths >2000 nm (Fig. 8).

4.2. Atmospheric compensation

Benefits of UAV include their deployability and thus are becoming very widely used for many applications under a wide range of conditions, therefore the analysis around atmospheric compensation is absolutely critical. Atmospheric compensation of HSI acquired below clouds is challenging because conventional radiative transfer model based corrections such as implemented in ATCOR assume a cloud free

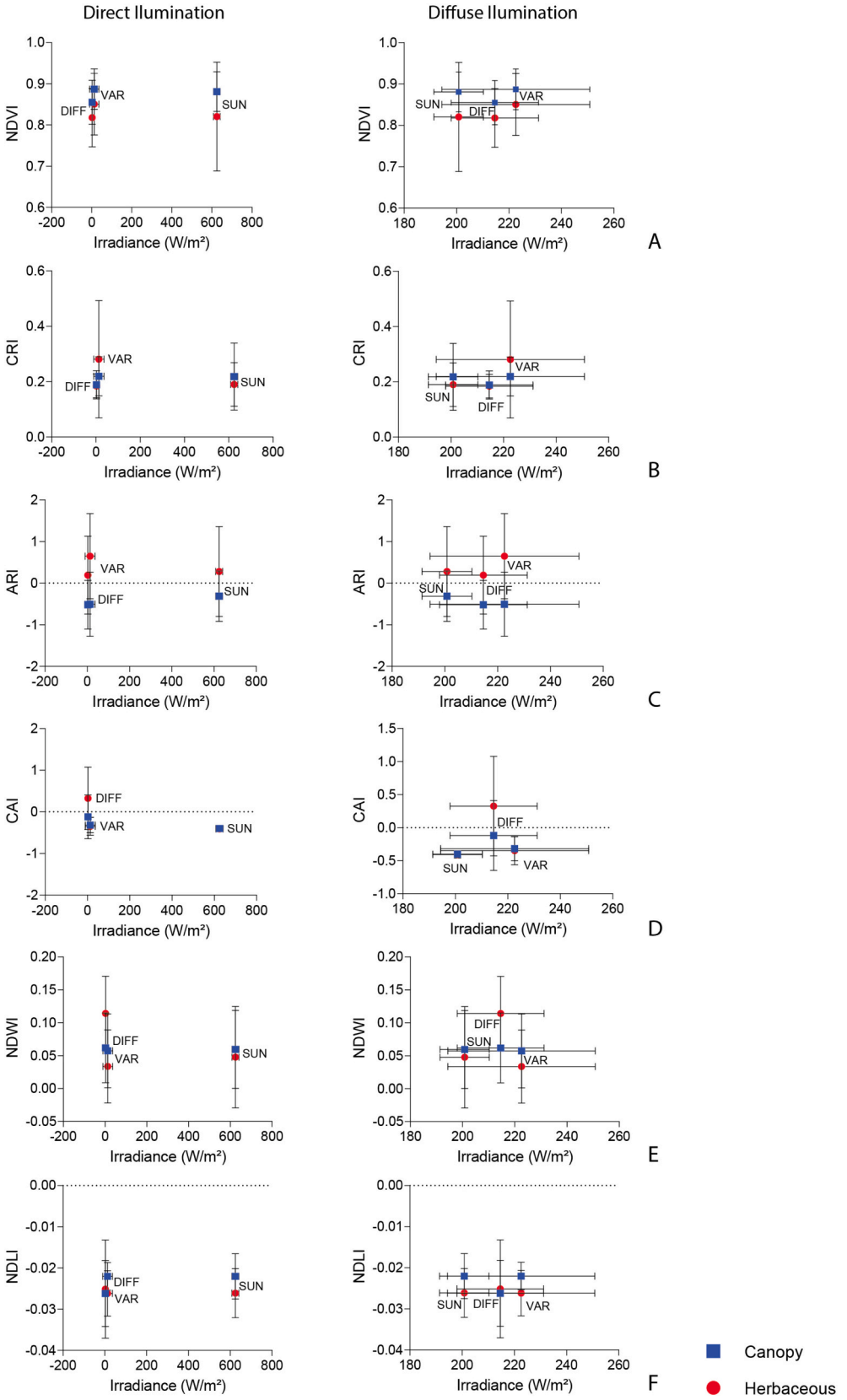

Fig. 12. Direct and diffuse illumination versus VNIR (A–C) and SWIR (D–F) SVIs for canopy and herbaceous vegetation across dates.

Table 7
Dunn's multiple comparisons test for SVIs across dates.

NDVI	Mean rank diff.	CAI	Mean rank diff.
SUN-CA vs. DIFF-CA*	1083	SUN-CA vs. DIFF-CA	−1416
SUN-CA vs. VAR-CA*	−239.8	SUN-CA vs. VAR-CA	−715.2
DIFF-CA vs. VAR-CA*	−1323	DIFF-CA vs. VAR-CA*	701.1
SUN-HE vs. DIFF-HE*	958.9	SUN-HE vs. DIFF-HE*	−2665
SUN-HE vs. VAR-HE	−150.4	SUN-HE vs. VAR-HE*	−660.1
DIFF-HE vs. VAR-HE*	−1109	DIFF-HE vs. VAR-HE*	2005
SUN-CA vs. SUN-HE*	1216	SUN-CA vs. SUN-HE*	259.3
DIFF-CA vs. DIFF-HE*	1092	DIFF-CA vs. DIFF-HE*	−989.5
VAR-CA vs. VAR-HE*	1305	VAR-CA vs. VAR-HE*	314.4
CRI		NDWI	
SUN-CA vs. DIFF-CA*	219.7	SUN-CA vs. DIFF-CA	−95.9
SUN-CA vs. VAR-CA*	−520.9	SUN-CA vs. VAR-CA	160.9
DIFF-CA vs. VAR-CA*	−740.5	DIFF-CA vs. VAR-CA	256.8
SUN-HE vs. DIFF-HE	32.41	SUN-HE vs. SUN-HE*	296.4
SUN-HE vs. VAR-HE*	−1229	SUN-HE vs. DIFF-HE*	−1648
DIFF-HE vs. VAR-HE*	−1261	SUN-HE vs. VAR-HE*	803
SUN-CA vs. SUN-HE*	523	SUN-CA vs. SUN-HE*	296.4
DIFF-CA vs. DIFF-HE*	335.7	DIFF-CA vs. DIFF-HE*	−1552
VAR-CA vs. VAR-HE	−185	VAR-CA vs. VAR-HE*	642.2
ARI		NDLI	
SUN-CA vs. DIFF-CA*	429.6	SUN-CA vs. DIFF-CA*	1047
SUN-CA vs. VAR-CA*	410.1	SUN-CA vs. VAR-CA	170.4
DIFF-CA vs. VAR-CA	−19.48	DIFF-CA vs. VAR-CA*	−876.6
SUN-HE vs. DIFF-HE	140.5	SUN-HE vs. DIFF-HE*	−1024
SUN-HE vs. VAR-HE*	−728.3	SUN-HE vs. VAR-HE	20.11
DIFF-HE vs. VAR-HE*	−868.8	DIFF-HE vs. VAR-HE*	1044
SUN-CA vs. SUN-HE*	−1364	SUN-CA vs. SUN-HE*	1270
DIFF-CA vs. DIFF-HE*	−1653	DIFF-CA vs. DIFF-HE*	−800.8
VAR-CA vs. VAR-HE*	−2503	VAR-CA vs. VAR-HE*	1120

CA = canopy leaves, HE = herbaceous vegetation.
* Difference is significant ($p < 0.05$).

atmosphere (Wright et al., 2020), and are not currently parameterized with the unique conditions imposed by predominantly diffuse irradiance (Fig. 4B) (Richter and Schlapfer, 2019). Radiative transfer models based on MODTRAN-5 rely on the retrieval of the aerosol optical thickness to calculate the visibility (horizontal meteorological range) which is related to the extinction coefficient at 550 nm (Richter and Schlapfer, 2019). The 550 nm band is also used in MODTRAN-5 to define a relationship between horizontal visibility and vertical optical thickness in clear sky conditions. A minimum SNR of 100:1 for dark targets has been shown to be adequate for aerosol optical thickness retrieval at 550 nm (Seidel et al., 2008). Retrieval over brighter targets requires a higher SNR (e.g. 300:1 at 30% reflectance). Vegetation is considered a low reflectivity target at 550 nm with a green peak reflectance generally less than 15%. For our HSI, the SNR was not high enough for the DIFF (SNR_{550nm} = 75:1) or VAR (SNR_{550nm} = 54:1) imagery to meet this requirement (Fig. 11). Only for the SUN imagery (SNR_{550nm} = 104:1) were the conditions favourable for a radiative transfer model approach. Also, an important consideration for imagery acquired below clouds is the multiple scattering between the ground and the clouds especially in wavelengths with higher reflectivity (e.g. NIR plateau of vegetation spectra) (Nann, 1990). These processes are not considered in conventional radiative transfer models. Therefore, for the DIFF and VAR imagery, an ELM compensation was required. For low altitude UAV-HSI, constant aerosol contents could be assumed due to the low aerosol variability and the short observation distance. Also, because below cloud conditions represent fully diffuse illumination, this result is less influence by scattered direct illumination. Therefore, the illumination field is much more homogeneous and measurements (such as ELM coefficients) can be transferred within the image with less error than would be encountered with high direct illumination.

The different approaches used for atmospheric compensation based on conditions at the time of acquisition is an important aspect to consider because our data collection reflects realistic fieldwork scenarios in an area where cloudy conditions are common, and resources need to be maximized. In addition to removing the majority of the atmospheric effects, both methods also resulted in a normalization of the differences in brightness seen in the radiance images most prominent in the DIFF and VAR imagery (Fig. 9). Refinement of the ELM taking into consideration the changes in the direct to diffuse ratio (e.g. Li et al., 2015) over the course of HSI acquisition may further improve the atmospheric compensation under highly variable illumination conditions. Future inclusion of a downwelling irradiance sensor onboard (e.g. Suomalainen et al., 2018) or coincident upwelling and downwelling irradiance measurements onboard (e.g. Wright et al., 2020) would further improve the results under varying illumination conditions and potentially further expand the utility of such imagery to other challenging conditions such as broken clouds.

When acquiring UAV-HSI in complex or restrictive environments where in-scattering from nearby objects cannot be avoided (Fig. 6), use of field spectroscopy measurements of contaminated targets for ELM or other corrections should be avoided. Including such errors into the processing chain will affect all subsequent analytics steps by modifying the spectra of pixels throughout the imagery resulting in a reduction in accuracy for analyses that require representative spectral signatures such as classification, target detection, modeling of traits from SVIs, etc. In this study the effects were mitigated by substituting the field spectra of the reference panels with their laboratory measured spectra. However, acquisition of coincident downwelling irradiance onboard, or a combination of upwelling and downwelling irradiance (e.g. Wright et al., 2020) would further mitigate these errors. In addition development of radiative transfer models that can account for the complex conditions in predominantly diffuse illumination would decrease the dependence on scene-based atmospheric compensation approaches in these situations.

4.3. SNR

The S-620 imager was operated in low gain mode for the duration of the acquisition. In future applications changing to high gain mode would likely improve the SNR under cloudy and low overall irradiance conditions. Nevertheless, for UAV-HSI, a trade-off between spatial resolution and SNR should be expected. Moderate resolution (30-90 m) spaceborne HSI acquiring data under clear or minimally cloudy conditions have been shown to have relatively high SNR, for example, Hyperion was shown to have an SNR of 150:1 at 650 nm (at 30% reflectance) (Buckingham et al., 2002; Peddle et al., 2008). Because of the much smaller pixels (< 5 cm) from UAV platforms, when operated in marginal atmospheric conditions, SNR is expected to be lower. Binning pixels in the along and/or across track direction will result in lower spatial resolution, but given the small native pixel sizes a degradation in spatial resolution may be a worthwhile trade-off for improved SNR (Jorge et al., 2017). As described in Fig. 3, the spatial binning of the V-1240 to match the image size of the S-620 results in an improvement in SNR by a factor of 3.3. However, further pixel summation of the combined VNIR-SWIR imagery could boost the SNR further for imagery acquired under diffuse conditions.

SNR requirements are application driven (Drusch et al., 2012; Nieke et al., 1998; Piscini and Amici, 2010) and of the various applications for which minimum SNR levels have been estimated (e.g. kaolinite doublet detection (Porter and Enmark, 1987), ocean color (Hu et al., 2012),

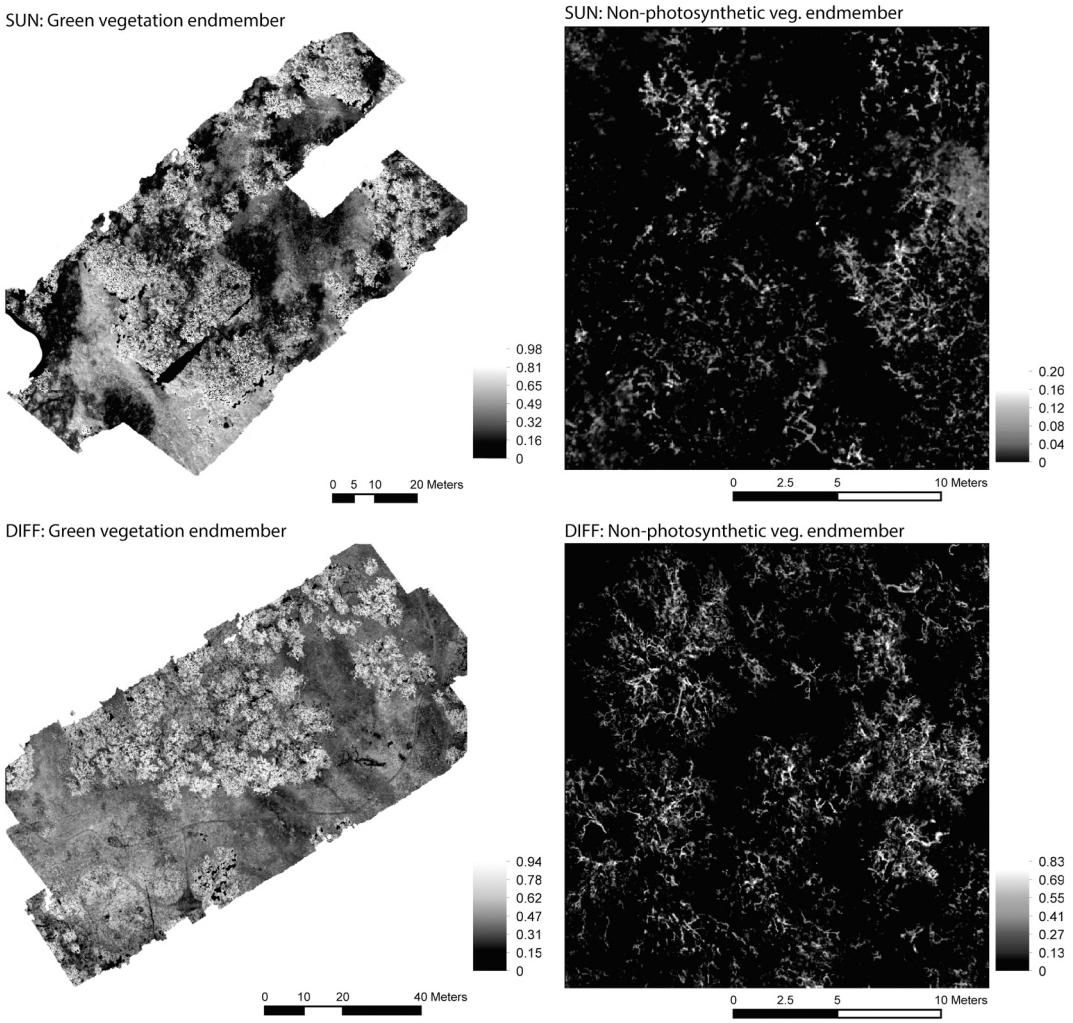

Fig. 13. Example of the most abundant endmembers from the two contrasting illumination conditions: predominantly direct illumination (SUN) and predominantly diffuse illumination (DIFF). Values in the legends represent proportional abundance (range 0–1).

essential aquatic biodiversity assessment (Muller-Karger et al., 2018)), vegetation applications are among the most sensitive (Peterson and Hubbard, 1992). Smith and Curran (1996) estimated the SNR requirements for the estimation of foliar biochemical concentrations from HSI finding minimum SNR values of 37:1 needed for Nitrogen retrieval, 50:1 for lignin and 65:1 for cellulose (from 1st derivative spectra). These values suggest that even under the lowest overall irradiance with the thickest cloud cover encountered with the DIFF imagery, the SNR is adequate for the retrieval of many foliar traits from features at wavelengths in the 550–1400 nm range (Fig. 10). It is important to note that once the effects of the atmosphere and other sensor geometry related characteristics are factored in (e.g. point spread function) (Inamdar et al., 2020) the requirement of SNR would likely increase and therefore care should be taken to limit the analyses to the wavelengths that meet the necessary SNR criteria.

4.4. SVIs

The variable wavelength attenuation by the clouds can be also clearly seen in the SVI results (Fig. 12). For tree canopy leaves, significant differences were found across illumination conditions for five of the six indices (Table 7, Fig. 12). Only NDWI (related to water content) was unaffected. For the herbaceous vegetation, all six indices showed significant differences across illumination conditions (Table 7, Fig. 12). While natural site-level variability is expected in the spectral response of the vegetation, the overall study area is small, therefore, the vegetation is likely exposed to similar precipitation, temperature, and edaphic conditions. There may be variability in the species composition of the herbaceous vegetation but the large sample size (1200–1500 pixels per class per image) minimized the effect of this variability on the SVI results. As well, some differences can be attributed to expected biological processes. For example, under diffuse illumination the herbaceous class has NDWI values indicative of higher water content than under high direct illumination potentially due to evapotranspiration differences. Nevertheless, depending on the wavelengths used to calculate the indices, the impact of the cloud cover will vary. For example, values of CAI from the DIFF and VAR imagery should be treated with caution due to the lower SNR at wavelengths >2000 nm and the residual noise seen in the data following atmospheric compensation (Figs. 7 and 8). Furthermore, when SVIs are calculated on surface reflectance imagery as intended, rather than digital counts or top of atmosphere reflectance, they have been shown to suppress topographic shading which is both consistent across bands in the visible to SWIR range and independent of surface material type (Jones and Vaughn, 2010) as opposed to variation in illumination, the effect of which is band dependent. Coburn et al. (2010) found a considerable anisotropic effects on both NDVI and the Water-Band-Index; estimates of vegetation characteristics derived from the SVIs could result in large errors depending on the illumination: viewing angle combination at time of data acquisition. Both macro (landscape) and micro (canopy structure) topographic effects can

strengthen BRDF effects in vegetation and are among the predominant sources of uncertainty in ecophysiological models from SVIs (Buchhorn et al., 2016). Our results show that similar magnitude differences can be found in SVIs due to the wavelength dependent attenuation by cloud cover. Therefore, care should be taken when comparing SVIs calculated under different illumination conditions, or when modeling traits or other variables from these indices because differences encountered may be due not only to site-level heterogeneity but also to the conditions under which the imagery was acquired. However, as discussed below, diffuse illumination conditions may minimize BRDF effects on SVIs and should be investigated further in mitigation of large uncertainties in vegetation trait estimation from SVIs in high latitudes with low sun angles (Buchhorn et al., 2016) and in areas with large seasonal solar angle variation (Breunig et al., 2015).

4.5. Endmember extraction

For the SUN image, the difference in abundance of the 'green leaf' endmember (Fig. 13) depending on whether the leaves are on the side of the canopy oriented facing the sun or on the opposite side is an artefact of the illumination condition rather than an actual difference in the foliage. However, imagery acquired under such conditions would be beneficial for examining the effects on spectral signatures from shadow gradation from the umbra to the penumbra. In contrast, class level spectral variability of the herbaceous vegetation was minimized in the SUN imagery. From the DIFF imagery, five of the most distinct endmembers are related to components of the meadow herbaceous vegetation. It therefore appears that under the diffuse illumination conditions environmental/biophysical differences in the herbaceous vegetation may be more readily differentiated. The prominence of the non-photosynthetic vegetation, mosses and lichens also differed in the endmember abundance, with up to four times higher values seen in the DIFF imagery. Lastly, the concept of "endmember" in ultra-high spatial resolution UAV-HSI merits consideration. When pixels represent very small cm-scale components of the landscape, it is likely that the majority are not "mixed pixels" as they would be from airborne or satellite platforms, therefore the interpretation of endmember identification algorithms will differ than from coarser scale airborne or satellite HSI.

5. Conclusion

To increase our understanding of imagery acquired by a full range pushbroom HSI (400–2500 nm) mounted on a UAV platform for ecosystem studies, we addressed three fundamental and interrelated aspects of UAV-HSI imagery acquired under various illumination conditions: atmospheric compensation, SNR and SVIs. In addition, we analyzed endmember identification results to illustrate the impact of diverse irradiance conditions on the spectra of vegetation. For atmospheric compensation we demonstrated that under high direct irradiance conditions, the MODTRAN-5 based radiative transfer model is applicable, consistent with Arroyo-Mora et al. (2019). However, under predominantly diffuse and variable irradiance conditions, an ELM approach was necessary. Moreover, regardless of illumination conditions, despite our best efforts to locate adequate placement for the reference calibration targets, in-scattering from nearby vegetation contaminated in-situ measurements of their absolute reflectance and these data were unsuitable as inputs into the ELM. In this case, we utilized laboratory determined spectral responses for the panels. This approach resulted in a high degree of similarity between spectra of the reference panels extracted from the pixels and the lab determined reference spectra. Under diffuse illumination conditions, the SWIR wavelength region should be used with caution due to both lower SNR and resultant increased noise in the spectra. Spatial and/or spectral binning of the raw data can be considered to increase the SNR under marginal atmospheric conditions. In addition, using a high gain mode during data acquisition would likely improve the signal quality under these conditions. Furthermore, wavelength and cloud characteristic dependant attenuation affects SVIs. Care must be taken in choosing an SVI in order for the interpretation to be relatable to biophysical phenomena rather than illumination. For instance, if the wavelengths used to calculate the SVI are affected similarly by τ and other cloud characteristics (e.g. droplet size), any resulting variability is more likely due to biophysical/chemical differences in the vegetation. SVIs have been broadly applied in the literature to imagery from many sensors at different spatial and spectral resolutions, however UAV-HSI do not have the same sensor characteristics as those for which the majority of these indices were developed (e.g. NDVI). Further, the ultra-high spatial resolution poses challenges in the interpretation of SVIs as related to biophysical/biochemical properties (e.g. chlorophyll concentration, water stress, etc.). New studies relating the sensitivity of UAV-HSI acquired under different illumination conditions to the estimation of in-situ vegetation biochemical traits are required. Similarly, our results demonstrate that well-known illumination derived phenomena such as the BRDF of vegetation which is shown to be accentuated under direct illumination obscures target biophysical variability. Diffuse illumination conditions may, therefore, be beneficial for determining structural and biochemical traits that otherwise would be obscured by commonly sought-after high direct illumination conditions and increase the spectral variability of the target.

Supplementary data to this article can be found online at https://doi.org/10.1016/j.rse.2021.112396.

Declaration of Competing Interest

The authors declare that they have no known competing financial interests or personal relationships that could have appeared to influence the work reported in this paper.

Acknowledgments

We would like to thank the Nature Conservancy of Canada for allowing us to conduct our research on their Cowichan Garry Oak Preserve site. We would also like to acknowledge Irv Banman for providing information relating to the historic land use of the site as well as Deep Inamdar, Kathryn Elmer, Erica Skye Schaaf, Patrick Osei Darko and Paul Hacker for their help in the field. This project was funded by the Natural Sciences and Engineering Research Council (NSERC) Discovery Frontiers grant to the Canadian Airborne Biodiversity Observatory (CABO). We thank three anonymous reviewers for their comments which improved the manuscript.

References

Aasen, H., Honkavaara, E., Lucieer, A., Zarco-Tejada, P., 2018. Quantitative remote sensing at ultra-high resolution with UAV spectroscopy: a review of sensor technology, measurement procedures, and data correction workflows. Remote Sens. 10, 1091.

Adams, J.B., Sabol, D.E., Kapos, V., Almeida Filho, R., Roberts, D.A., Smith, M.O., Gillespie, A.R., 1995. Classification of multispectral images based on fractions of endmembers: application to land-cover change in the Brazilian Amazon. Remote Sens. Environ. 52, 137–154.

Arroyo-Mora, J.P., Kalacska, M., Inamdar, D., Soffer, R., Lucanus, O., Gorman, J., Naprstek, T., Schaaf, E.S., Ifimov, G., Elmer, K., Leblanc, G., 2019. Implementation of a UAV–hyperspectral Pushbroom imager for ecological monitoring. Drones 3, 12.

Asner, G.P., 2001. Cloud cover in Landsat observations of the Brazilian Amazon. Int. J. Remote Sens. 22, 3855–3862.

Banerjee, B.P., Raval, S., Cullen, P.J., 2020. UAV-hyperspectral imaging of spectrally complex environments. Int. J. Remote Sens. 41, 4136–4159.

Bartlett, J.S., Ciotti, A.M., Davis, R.F., Cullen, J.J., 1998. The spectral effects of clouds on solar irradiance. J. Geophys. Res. 103, 31017–31031.

Basnet, B., Vodacek, A., 2015. Tracking land use/land cover dynamics in cloud prone areas using moderate resolution satellite data: a case study in Central Africa. Remote Sens. 7, 6683–6709.

Beamish, A.L., Coops, N.C., Hermosilla, T., Chabrillat, S., Heim, B., 2018. Monitoring pigment-driven vegetation changes in a low-Arctic tundra ecosystem using digital cameras. Ecosphere 9, e02123.

Berg, L.K., Kassianov, E.I., Long, C.N., Mills Jr., D.L., 2011. Surface summertime radiative forcing by shallow cumuli at the Atmospheric Radiation Measurement Southern Great Plains site. J. Geophys. Res. 116.
Black, M., Fleming, A., Riley, T., Ferrier, G., Fretwell, P., McFee, J., Achal, S., Diaz, A.U., 2014. On the atmospheric correction of Antarctic airborne hyperspectral data. Remote Sens. 6, 4498–4514.
Breunig, F.M., Galvao, L.S., dos Santos, J.R., Gitelson, A.A., de Moura, Y.M., Teles, T.S., Gaida, W., 2015. Spectral anisotropy of subtropical deciduous forest using MISR and MODIS data acquired under large seasonal variation in solar zenith angle. Int. J. Appl. Earth Obs. Geoinf. 35, 294–304.
Buchhorn, M., Raynolds, M.K., Walker, D.A., 2016. Influence of BRDF on NDVI and biomass estimations of Alaska Arctic tundra. Environ. Res. Lett. 11, 12.
Buckingham, R., Staenz, K., Hollinger, A., 2002. Review of Canadian airborne and space activities in hyperspectral remote sensing. Can. Aeronaut. Space J. 48, 115–121.
Burkart, A., Aasen, H., Alonso, L., Menz, G., Bareth, G., Rascher, U., 2015. Angular dependency of hyperspectral measurements over wheat characterized by a novel UAV based goniometer. Remote Sens. 7, 725–746.
Coburn, C.A., Van Gaalen, E., Peddle, D.R., Flanagan, L.B., 2010. Anisotropic reflectance effects on spectral indices for estimating ecophysiological parameters using a portable goniometer system. Can. J. Remote. Sens. 36, S355–S364.
Drusch, M., Del Bello, U., Carlier, S., Colin, O., Fernandez, V., Gascon, F., Hoersch, B., Isola, C., Laberinti, P., Martimort, P., Meygret, A., Spoto, F., Sy, O., Marchese, F., Bargellini, P., 2012. Sentinel-2: ESA's optical high-resolution mission for GMES operational services. Remote Sens. Environ. 120, 25–36.
Eismann, M.T., GOES-R Program Office, 2012. Hyperspectral remote sensing. SPIE Press, Bellingham, WA, USA.
Elmer, K., Soffer, R.J., Arroyo-Mora, J.P., Kalacska, M., 2020. ASDToolkit: a novel MATLAB processing toolbox for ASD field spectroscopy data. Data 5, 96.
Evans, W.F.J., Puckrin, E., 2003. The absorption of NIR solar radiation by precipitating clouds. In: 14th Symposium on Global Change and Climate Long Beach, CA.
Frantz, D., Haß, E., Uhl, A., Stoffels, J., Hill, J., 2018. Improvement of the Fmask algorithm for Sentinel-2 images: separating clouds from bright surfaces based on parallax effects. Remote Sens. Environ. 215, 471–481.
Freitas, S., Silva, H., Almeida, J., Silva, E., 2018. Hyperspectral imaging for real-time unmanned aerial vehicle maritime target detection. J. Intel. Robot. Syst. 90, 551–570.
Fuchs, M.A., 2001. Towards a recovery strategy for Garry oak and associated ecosystems in Canada: ecological assessment and literature review. In: C.W.S. Technical Report GBEI/EC-00-030. Environment Canada, Pacific and Yukon Region.
Gamon, J.A., Field, C.B., Goulden, M.L., Griffin, K.L., Hartley, A.E., Joel, G., Penuelas, J., Valentini, R., 1995. Relationships between NDVI, canopy structure, and photosynthesis in three Californian vegetation types. Ecol. Appl. 5, 28–41.
Gao, B.-C., 1996. NDWI—a normalized difference water index for remote sensing of vegetation liquid water from space. Remote Sens. Environ. 58, 257–266.
Giardino, C., Bresciani, M., Valentini, E., Gasperini, L., Bolpagni, R., Brando, V.E., 2015. Airborne hyperspectral data to assess suspended particulate matter and aquatic vegetation in a shallow and turbid lake. Remote Sens. Environ. 157, 48–57.
Giles, J.H., Ridder, T.D., Williams, R.H., Jones, D.A., Denton, M.B., 1998. Product review: selecting a CCD camera. Anal. Chem. 70, 663A–668A.
Gitelson, A.A., Zur, Y., Chivkunova, O.B., Merzlyak, M.N., 2002. Assessing carotenoid content in plant leaves with reflectance spectroscopy. Photochem. Photobiol. 75 (3), 272–281.
Gitelson, A.A., Merzlyak, M.N., Chivkunova, O.B., 2001. Optical properties and nondestructive estimation of anthocyanin content in plant leaves. Photochem. Photobiol. 74, 38–45.
GOES-R Algorithm Working Group, GOES-R Program Office, 2018. NOAA GOES-R Series Advanced Baseline Imager (ABI) Level 2 Cloud Optical Depth (COD). NOAA National Centers for Environmental Information.
Goetz, A., Calvin, W., 1987. Imaging Spectrometry: Spectral Resolution and Analytical Identification of Spectral Features. SPIE.
Gruninger, J., Ratkowski, A., Hoke, M., 2004. The Sequential Maximum Angle Convex Cone (SMACC) Endmember Model. SPIE.
Hakala, T., Honkavaara, E., Saari, H., Mäkynen, J., Kaivosoja, J., Pesonen, L., Pölönen, I., 2013. Spectral imaging from UAVs under varying illumination conditions. Int. Arch. Photogramm. Remote Sens. Spatial Inf. Sci. 189–194. XL-1/W2.
Heidinger, A.K., Li, Y., Wanzong, S., Noh, Y.J., Walther, A., Tushaus, S., Miller, S., 2018. 7.05 - satellite remote sensing of cloud vertical structure. In: Liang, S. (Ed.), Comprehensive Remote Sensing. Elsevier, Oxford, pp. 97–136.
Heli, T.H., 2006. Characterization of digital image noise properties based on RAW data. In: Proc.SPIE.
Honkavaara, E., Khoramshahi, E., 2018. Radiometric correction of close-range spectral image blocks captured using an unmanned aerial vehicle with a radiometric block adjustment. Remote Sens. 10, 256.
Honkavaara, E., Saari, H., Kaivosoja, J., Pölönen, I., Hakala, T., Litkey, P., Mäkynen, J., Pesonen, L., 2013. Processing and assessment of spectrometric, stereoscopic imagery collected using a lightweight UAV spectral camera for precision agriculture. Remote Sens. 5, 5006–5039.
Hu, C., Feng, L., Zhongping, L., Curtiss, O.D., Mannino, A., McClain, C.R., Franz, B.A., 2012. Dynamic range and sensitivity requirements of satellite ocean color sensors: learning from the past. Appl. Opt. 51, 6045–6062.
Inamdar, D., Kalacska, M., Leblanc, G., Arroyo-Mora, J., 2020. Characterizing and mitigating sensor generated spatial correlations in airborne hyperspectral imaging data. Remote Sens. 12.
Jones, H.G., Vaughn, R.A., 2010. Remote Sensing of Vegetation. Oxford Univesity Press, New York, NY.
Jorge, D.S.F., Barbosa, C.C.F., De Cavalho, L.A.S., Affonso, A.G., Lobo, F.D.L., Novo, E.M. L.D.M., 2017. SNR (signal-to-noise ratio) impact on water constituent retrieval from simulated images of optically complex Amazon Lakes. Remote Sens. 9.
Kalacska, M., Chmura, G.L., Lucanus, O., Bérubé, D., Arroyo-Mora, J.P., 2017. Structure from motion will revolutionize analyses of tidal wetland landscapes. Remote Sens. Environ. 199, 14–24.
Kalacska, M., Lucanus, O., Arroyo-Mora, J.P., Laliberté, É., Elmer, K., Leblanc, G., Groves, A., 2020. Accuracy of 3D landscape reconstruction without ground control points using different UAS platforms. Drones 4, 13.
King, M.D., Platnick, S., Menzel, W.P., Ackerman, S.A., Hubanks, P.A., 2013. Spatial and temporal distribution of clouds observed by MODIS onboard the terra and aqua satellites. IEEE Trans. Geosci. Remote Sens. 51, 3826–3852.
Koirala, P., Løke, T., Baarstad, I., Fridman, A., Hernandez, J., 2017. Real-time Hyperspectral Image Processing for UAV Applications, Using HySpex Mjolnir-1024. SPIE.
Lambert, T.J., Waters, J.C., 2014. Chapter 3 - assessing camera performance for quantitative microscopy. In: Waters, J.C., Wittman, T. (Eds.), Methods in Cell Biology. Academic Press, pp. 35–53.
Levy, C.R., Burakowski, E., Richardson, A.D., 2018. Novel measurements of fine-scale albedo: using a commercial quadcopter to measure radiation fluxes. Remote Sens. 10, 1303.
Li, H., Zhang, H., Zhang, B., Chen, Z., Yang, M., Zhang, Y., 2015. A method suitable for vicarious calibration of a UAV hyperspectral remote sensor. IEEE J. Select. Topics Appl. Earth Observ. Remote Sens. 8, 3209–3223.
Lubin, D., Vogelmann, A.M., 2011. The influence of mixed-phase clouds on surface shortwave irradiance during the Arctic spring. J. Geophys. Res. 116.
Lucanus, O., Kalacska, M., 2020. UAV DSLR Photogrammetry With PPK Processing.
Lucieer, A., Malenovský, Z., Veness, T., Wallace, L., 2014. HyperUAS—imaging spectroscopy from a multirotor unmanned aircraft system. J. Field Robot. 31, 571–590.
Manolakis, D.G., Lockwood, R.B., Cooley, T.W., 2016. The remote sensing environment. In: Hyperspectral Imaging Remote Sensing: Physics, Sensors, and Algorithms. Cambridge University Press, Cambridge, pp. 36–116.
Markelin, L., Simis, S.G.H., Hunter, P.D., Spyrakos, E., Tyler, A.N., Clewley, D., Groom, S., 2017. Atmospheric correction performance of hyperspectral airborne imagery over a small eutrophic lake under changing cloud cover. Remote Sens. 9, 2.
McCune, J.L., Pellatt, M.G., Vellend, M., 2013. Multidisciplinary synthesis of long-term human–ecosystem interactions: A perspective from the Garry oak ecosystem of British Columbia. Biol. Conserv. 166, 293–300.
McMinn, R.G., Eis, S., Hirvonen, H.E., Oswald, E.T., Senyk, J.P., 1976. Native vegetation in British Columbia's capital region. In: P.F.R.C. Government of Canada (Ed.), Information Report BC-X-140. Department of the Environment. Canadian Forest Service, Victoria, BC (18 pp.).
Mecikalski, J.R., Minnis, P., Palikonda, R., 2013. Use of satellite derived cloud properties to quantify growing cumulus beneath cirrus clouds. Atmos. Res. 120-121, 192–201.
Meyer, D., Verstraete, M., Pinty, B., 1995. The effect of surface anisotropy and viewing geometry on the estimation of NDVI from AVHRR. Remote Sens. Rev. 12, 3–27.
Milton, E.J., Schaepman, M.E., Anderson, K., Kneubühler, M., Fox, N., 2009. Progress in field spectroscopy. Remote Sens. Environ. 113, S92–S109.
Miyauchi, M., 1985. Properties of diffuse solar radiation under overcast skies with stratified cloud II. Spectral distribution. J. Meteorol. Soc. Jpn. 64, 1083–1095.
Moses, W.J., Bowles, J.H., Lucke, R.L., Corson, M.R., 2012. Impact of signal-to-noise ratio in a hyperspectral sensor on the accuracy of biophysical parameter estimation in case II waters. Opt. Express 20, 4309–4330.
Muller-Karger, F.E., Hestir, E., Ade, C., Turpie, K., Roberts, D.A., Siegel, D., Miller, R.J., Humm, D., Izenberg, N., Keller, M., Morgan, F., Frouin, R., Dekker, A.G., Gardner, R., Goodman, J., Schaeffer, B., Franz, B.A., Pahlevan, N., Mannino, A.G., Concha, J.A., Ackleson, S.G., Cavanaugh, K.C., Romanou, A., Tzortziou, M., Boss, E.S., Pavlick, R., Freeman, A., Rousseaux, C.S., Dunne, J., Long, M.C., Klein, E., McKinley, G.A., Goes, J., Letelier, R., Kavanaugh, M., Roffer, M., Bracher, A., Arrigo, K.R., Dierssen, H., Zhang, X., Davis, F.W., Best, B., Guralnick, R., Moisan, J., Sosik, H.M., Kudela, R., Mouw, C.B., Barnard, A.H., Palacios, S., Roesler, C., Drakou, E.G., Appeltans, W., Jetz, W., 2018. Satellite sensor requirements for monitoring essential biodiversity variables of coastal ecosystems. Ecol. Appl. 28, 749–760.
Nagler, P.L., Inoue, Y., Glenn, E.P., Russ, A.L., Daughtry, C.S.T., 2003. Cellulose absorption index (CAI) to quantify mixed soil–plant litter scenes. Remote Sens. Environ. 87, 310–325.
Nann, S., 1990. A cloud cover modifier for solar spectral irradiance modelling. In: Horigome, T., Kimura, K., Takakura, T., Nishino, T., Fujii, I. (Eds.), Clean and Safe Energy Forever. Pergamon, Oxford, pp. 422–426.
Nicodemus, F.E., Richmond, J.C., Hsia, J.J., Ginsberg, I.W., Limperis, T., 1977. Geometrical considerations and nomenclature for reflectance. In: Final Report National Bureau of Standards.
Nicolas, S., Baarstad, I., 2019. HySpex Mjolnir S-620 Hyperspectral Camera Test Report. HySpex NEO, Skedsmokorset Norway.
Nieke, J., Solbrig, M., Neumann, A., 1998. Signal-to-noise ratio reduction due to image smear concerning spaceborne imaging spectrometers for remote sensing of the Earth. In: Proc.SPIE.
Pecenak, Z.K., Mejia, F.A., Kurtz, B., Evan, A., Kleissl, J., 2016. Simulating irradiance enhancement dependence on cloud optical depth and solar zenith angle. Sol. Energy 136, 675–681.
Peddle, D.R., Boulton, R.B., Pilger, N., Bergeron, M., Hollinger, A., 2008. Hyperspectral detection of chemical vegetation stress: evaluation for the Canadian HERO satellite mission. Can. J. Remote. Sens. 34, S198–S216.
Peterson, D.L., Hubbard, G.S., 1992. Scientific issues and potential remote-sensing requirements for plant biochemical content. J. Imag. Sci. Technol. 36, 446–456.

Piscini, A., Amici, S., 2010. Estimation of signal to noise for unsupervised hyperspectral images. Q. Geofis. 78, 4–12.
Porter, W., Enmark, H., 1987. A System Overview of the Airborne Visible/Infrared Imaging Spectrometer (Aviris). SPIE.
Potgieter, A.B., George-Jaeggli, B., Chapman, S.C., Laws, K., Suárez Cadavid, L.A., Wixted, J., Watson, J., Eldridge, M., Jordan, D.R., Hammer, G.L., 2017. Multi-spectral imaging from an unmanned aerial vehicle enables the assessment of seasonal leaf area dynamics of sorghum breeding lines. Front. Plant Sci. 8.
Ranquist, E., Steiner, M., Argrow, B., 2017. Exploring the range of weather impacts on UAS operations. In: 18th Conference on Aviation, Range and Aerospace Meteorology, At Seattle, WA.
Richter, R., 1996. Atmospheric correction of satellite data with haze removal including a haze/clear transition region. Comput. Geosci. 22, 675–681.
Richter, R., Schläpfer, D., 2002. Geo-atmospheric processing of airborne imaging spectrometry data. Part 2: atmospheric/topographic correction. Int. J. Remote Sens. 23, 2631–2649.
Richter, R., Schlapfer, D., 2019. Atmopsheric / Topographic Correction for Airborne Imagery. ATCOR-4 User Guide, Version 7.0.3. DLR / ReSe, Wessling, DLR-IB 565-02, p. 257. https://www.rese-apps.com/pdf/atcor4_manual.pdf.
Richter, R., Schläpfer, D., Müller, A., 2011. Operational atmospheric correction for imaging spectrometers accounting for the smile effect. IEEE Trans. Geosci. Remote Sens. 49, 1772–1780.
Rouse Jr., J.W., Haas, R.H., Schell, J.A., Deering, D.W., 1974. Monitoring Vegetation Systems in the Great Plains with Erts. NASA Special Publication, p. 309.
Ruwaimana, M., Satyanarayana, B., Otero, V., Muslim, M., Syafiq, A.M., Ibrahim, S., Raymaekers, D., Koedam, N., Dahdouh-Guebas, F., 2018. The advantages of using drones over space-borne imagery in the mapping of mangrove forests. PLoS One 13, e0200288.
Sano, E.E., Ferreira, L.G., Asner, G.P., Steinke, E.T., 2007. Spatial and temporal probabilities of obtaining cloud-free Landsat images over the Brazilian tropical savanna. Int. J. Remote Sens. 28, 2739–2752.
Schläpfer, D., 2018. Parametric Geocoding (PARGE). ReSe Applications LLC. https://www.rese-apps.com/software/parge/index.html.
Schläpfer, D., Richter, R., 2002. Geo-atmospheric processing of airborne imaging spectrometry data. Part 1: parametric orthorectification. Int. J. Remote Sens. 23, 2609–2630.
Seidel, F., Schläpfer, D., Nieke, J., Itten, K.I., 2008. Sensor performance requirements for the retrieval of atmospheric aerosols by airborne optical remote sensing. Remote Sens. 8, 1901–1914.
Serrano, L., Peñuelas, J., Ustin, S.L., 2002. Remote sensing of nitrogen and lignin in Mediterranean vegetation from AVIRIS data: decomposing biochemical from structural signals. Remote Sens. Environ. 81, 355–364.
Smith, G.M., Curran, P.J., 1996. The signal-to-noise ratio (SNR) required for the estimation of foliar biochemical concentrations. Int. J. Remote Sens. 17, 1031–1058.
Smith, G.M., Milton, E.J., 1999. The use of the empirical line method to calibrate remotely sensed data to reflectance. Int. J. Remote Sens. 20, 2653–2662.
Soffer, R., 2014. Contamination of ground spectral measurements due to operator proximity. In: IGARSS 2014 / 35th Canadian Symposium on Remote Sensing, Quebec, Canada.
Soffer, R.J., Ifimov, G., Arroyo-Mora, J.P., Kalacska, M., 2019. Validation of airborne hyperspectral imagery from laboratory panel characterization to image quality assessment: implications for an Arctic peatland surrogate simulation site. Can. J. Remote. Sens. 45, 476–508.
Suomalainen, J., Hakala, T., de Oliveira, R.A., Markelin, L., Viljanen, N., Nasi, R., Honkavaara, E., 2018. A novel tilt correction technique for irradiance sensors and spectrometers on-board unmanned aerial vehicles. Remote Sens. 10, 18.
Walther, A., Straka, W., Heidinger, A.K., 2013. ABI Algorithm Theoretical Basis Document For Daytime Cloud Optical and Microphysical Properties (DCOMP) Version 3.0.
Wang, S., Baum, A., Zarco-Tejada, P.J., Dam-Hansen, C., Thorseth, A., Bauer-Gottwein, P., Bandini, F., Garcia, M., 2019. Unmanned aerial system multispectral mapping for low and variable solar irradiance conditions: potential of tensor decomposition. ISPRS J. Photogramm. Remote Sens. 155, 58–71.
Wendel, A., Underwood, J., 2017. Illumination compensation in ground based hyperspectral imaging. ISPRS J. Photogramm. Remote Sens. 129, 162–178.
Wierzbicki, D., Kedzierski, M., Fryskowska, A., 2015. Assesment of the influence of UAV image quality on the orthophoto production. In: ISPRS - International Archives of the Photogrammetry, Remote Sensing and Spatial Information Sciences, XL-1/W4, pp. 1–8.
Wright, L.A., Kindel, B., Pilewski, P., Leisso, N., Kampe, T.U., Schmidt, K.S., 2020. Below-cloud atmospheric compensation of airborne hypespectral imagery using simultaneous solar spectral irradiance observations. In: Ieee Transactions on Geoscience and Remote Sensing.
Yao, X., Wang, N., Liu, Y., Cheng, T., Tian, Y., Chen, Q., Zhu, Y., 2017. Estimation of wheat LAI at middle to high levels using unmanned aerial vehicle narrowband multispectral imagery. Remote Sens. 9, 1304.
Zarco-Tejada, P.J., Guillén-Climent, M.L., Hernández-Clemente, R., Catalina, A., González, M.R., Martín, P., 2013. Estimating leaf carotenoid content in vineyards using high resolution hyperspectral imagery acquired from an unmanned aerial vehicle (UAV). Agric. For. Meteorol. 171–172, 281–294.
Zare, A., Ho, K., 2014. Endmember variability in hyperspectral analysis: addressing spectral variability during spectral unmixing. In: Signal Processing Magazine, 31. IEEE, pp. 95–104.
Zhang, L., Du, B., 2012. Recent advances in hyperspectral image processing. Geo-spat. Inform. Sci. 15, 143–156.
Zhu, Z., Woodcock, C.E., 2012. Object-based cloud and cloud shadow detection in Landsat imagery. Remote Sens. Environ. 118, 83–94.